METAL OXIDE SORBENTS FOR CARBON DIOXIDE CAPTURE PREPARED BY ULTRASONIC SPRAY PYROLYSIS

BY

BRANDON R. ITO

THESIS

Submitted in partial fulfillment of the requirements
for the degree of Master of Science in Chemistry
in the Graduate College of the
University of Illinois at Urbana-Champaign, 2011

Urbana, Illinois

Advisor:

Professor Kenneth S. Suslick

ABSTRACT

Over the past 60 years, there has been a dramatic increase in the amount of carbon dioxide in the atmosphere. The rising CO_2 levels can be traced to anthropogenic sources, the majority of which comes from burning fossil fuels for power generation. As a result, research is underway to incorporate CO_2 capture into power plants using the integrated gasification combined cycle (IGCC), which is a method for cleaning flue gas produced from gasified coal.

Presently, the lack of a cost-effective CO_2 adsorbent is preventing the integration of CO_2 capture into IGCC plants. There is much work being done on many classes of materials to solve this problem including supported amines, zeolites, activated carbons, metal oxides, lithium zirconates, hydrotalcites, and metal-organic frameworks. In the metal oxide class, calcium oxide is emerging as an attractive sorbent because it has a high capacity for CO_2 (17.8 mmol g^{-1}), is abundant in the form of limestone, and adsorbs CO_2 at high temperatures, which can reduce costs by eliminating cooling of the gas for CO_2 capture.

Here, the results of CaO materials synthesized by ultrasonic spray pyrolysis (USP) are presented. It is shown that the morphology of USP-synthesized CaO sorbents can be easily controlled but that there is little difference between each sorbent in cyclic carbonation/calcination stability. Sorbents synthesized via USP, however, perform better than commercially available $CaCO_3$. Finally, the effects of adding aluminum or magnesium binder phases on the cyclic stability and capacity of the sorbents are reported to greatly improve sorbent stability over 15 cycles.

TABLE OF CONTENTS

List of Figures vi

List of Tables ix

Chapter 1: Capturing Anthropogenic Carbon Dioxide 1

1.1 The Carbon Dioxide Issue 1

1.2 The Integrated Gasification Combined Cycle 4

1.3 Sorbents for Carbon Dioxide Capture 5

1.3.1 Amine-based Sorbents 6

1.3.2 Zeolites.. 9

1.3.3 Activated Carbons 13

1.3.4 Metal Oxides 15

1.3.5 Lithium Zirconates 16

1.3.6 Hydrotalcites 19

1.3.7 Metal-Organic Frameworks 21

1.4 Summary 22

1.5 References 22

Chapter 2: Experimental Methods 36

2.1 Ultrasonic Spray Pyrolysis 36

2.2 Apparatus 37

2.3 Solution Preparation 40

2.4 Product Collection and Isolation 40

2.5 Materials Characterization 41
2.5.1 Scanning Electron Microscopy. 41
2.5.2 Transmission Electron Microscopy 41
2.5.3 Powder X-ray Diffraction 41
2.5.4 Surface Area Analysis 42
2.5.5 Thermogravametric Analysis 42
2.6 References 43

Chapter 3: Hollow, Porous Calcium Oxide Prepared by Ultrasonic Spray Pyrolysis 45
3.1 Introduction 45
3.1.1 Calcium Oxide 45
3.1.2 Modeling Sorbent Degradation 47
3.1.3 Binders and Supports for Calcium Oxide 49
3.1.4 Effects of Hydration 49
3.2 Experimental 50
3.2.1 Materials and Equipment 50
3.2.2 Preparation of Hollow Calcium Carbonate by USP 50
3.2.3 Preparation of Al-doped Calcium Carbonate by USP 51
3.2.4 Preparation of Mg-doped Calcium Carbonate by USP. 51
3.3 Results and Discussion 52
3.3.1 Experimental Design 52
3.3.1.1 Hollow Morphology 52
3.3.1.2 Precursor Selection 53

3.3.1.3 Solvent Selection 53
3.3.1.4 Cycling Conditions on the TGA 55
3.3.2 Control Over Calcium Carbonate Structure 57
3.3.2.1 Effect of Furnace Temperature 57
3.3.2.2 Effect of Precursor Solution Concentration 58
3.3.2.3 Effect of Precursor Solvent Composition 59
3.3.2.4 Effect of Structure on Sorbent Stability 61
3.3.3 CaO Sorbents Synthesized with Binders 64
3.3.3.1 Mayenite Binder 64
3.3.3.2 Magnesium Oxide Binder 70
3.4 Summary 72
3.5 References 72

LIST OF FIGURES

Figure 1.1 Seasonal trend (red line) and corrected average trend (black line) of atmospheric carbon dioxide over the past 60 years. 2

Figure 1.2 (A) Total US greenhouse gas emissions in 2009. **(B)** US carbon dioxide emissions by sector. *High-global warming potential gases 2

Figure 1.3 Diagram of the integrated gasification combined cycle with carbon dioxide capture 4

Figure 1.4 Data for six different anchored amine sorbents cycled under **(A)** dry conditions and **(B)** humid conditions (74% relative humidity at 25 °C). 8

Figure 1.5 The structure of faujasite. The roman numerals indicate locations where cations typically reside. 9

Figure 1.6 The effect of temperature on carbon dioxide and nitrogen adsorption curves on zeolite 13X. 1 bar = 14.5 psi 10

Figure 1.7 The effect of varying the Si:Al ratio in zeolites MCM-22 and MCM-49. 11

Figure 1.8 The effect of temperature at various pressures on the adsorption capacity of activated carbons. 14

Figure 1.9 (A) Mechanism of the formation of a lithium carbonate shell around pure lithium zirconate. **(B)** Formation of a molten lithium carbonate shell upon the addition of potassium allowing faster diffusion to the particle center. 17

Figure 1.10 The effect of the presence of water on the capture capacity of a hydrotalcite 20

Figure 1.11 The carbon dioxide capture capacity of various MOFs as a function of pressure. 21

Figure 2.1 Mechanism for the formation of hollow particles via USP. 37

Figure 2.2 Scheme of the USP apparatus 38

Figure 2.3 (A) Parts of the custom clamp and **(B)** the custom clamp assembled for USP. 1 = base brass ring, 2 = O-ring, 3 = polyethylene membrane (2 mils), 4 = nebulization cell, 5 = Teflon pieces, 6 = brass pieces, 7 = washers and nuts. 39

Figure 2.4 Diagram of the method programed for multiple carbonation/calcination cycles. Red corresponds to heating, black to isothermal periods under N_2, blue to cooling, and green to isothermal periods under CO_2. 43

Figure 3.1 Typical CO_2 capture curve for CaO. Carbonated at 600 °C in 100% CO_2. ...46

Figure 3.2 Several studies on the degradation of CaO sorbent capacity for CO_2 over multiple cycles from the work of Curran, Barker, Silaban, Aihara, Shimizu, Deutsch, and the equation proposed by Abanades. Data compiled by Abanades 48

Figure 3.3 Diagram of particle expansion both inward and outward for hollow particles 52

Figure 3.4 SEM images of calcium products made by USP. **(A)** Synthesized from an aqueous solution and collected in the bubblers. **(B)** Synthesized from an aqueous solution and collected from the furnace tube. **(C)** Synthesized from an ethanol solution and collected in the bubblers. 54

Figure 3.5 XRD of $CaCO_3$ isolated from the USP bubblers. 54

Figure 3.6 Effect of the cycling conditions on USP $CaCO_3$ cyclic stability after 15 cycles. 56

Figure 3.7 TEM images of USP $CaCO_3$ synthesized at different furnace temperatures: **(A)** 600 °C, **(B)** 700°C, and **(C)** 800 °C. 58

Figure 3.8 TEM images of USP $CaCO_3$ synthesized from **(A)** 0.125 M, **(B)** 0.25 M, and **(C)** 0.50 M solutions of $Ca(NO_3)_2 \cdot 4H_2O$ in 95% ethanol. 59

Figure 3.9 TEM images showing the effect on USP $CaCO_3$ particle structure of varying amounts of water in the ethanol precursor solution. **(A)** 0% H_2O. **(B)** 6.7% H_2O. **(C)** 10% H_2O. **(D)** 20% H_2O. 59

Figure 3.10 The sorbent stability of USP $CaCO_3$ synthesized from different precursor solutions. 62

Figure 3.11 SEM images of the USP $CaCO_3$ sorbent. **(A)** Low magnification before cycling. **(B)** Low magnification after 15 cycles. **(C)** High magnification before cycling. **(D)** High magnification after 15 cycles 63

Figure 3.12 Sorbent stability of USP $CaCO_3$ compared to two commercial $CaCO_3$ samples. 63

Figure 3.13 XRD patterns of 75:25 Al-sorbent **(A)** before and **(B)** after calcination. 65

Figure 3.14 XRD of the 0:100 Al-sorbent. 66

Figure 3.15 TEM images of Al-containing sorbents with various CaO:$Ca_{12}Al_{14}O_{33}$ wt% ratios. **(A)** 100:0. **(B)** 95:5. **(C)** 85:15. **(D)** 75:25. **(E)** 65:35. **(F)** 50:50. **(G)** 35:65. **(H)** 0:100. 67

Figure 3.16 Graphs of the Al-containing sorbents showing **(A)** sorbent capacity and **(B)** sorbent stability over 15 cycles. Cycle zero represents the theoretical capacity 69

Figure 3.17 SEM images of the 75:25 Al-sorbent. **(A)** Low magnification before cycling. **(B)** Low magnification after 15 cycles. **(C)** High magnification before cycling. **(D)** High magnification after 15 cycles. 69

Figure 3.18 Total CO_2 captured per gram of each Al-containing sorbent. 70

Figure 3.19 XRD of the 75:25 Mg-sorbent. 71

Figure 3.20 (A) Comparison of the 75:25 Al-sorbent and the 75:25 Mg-sorbent. **(B)** Enlarged for clear distinction. 72

LIST OF TABLES

Table 3.1 Conditions under which USP $CaCO_3$ was synthesized for TGA cycling. *Standard Liter Per Minute. 55

Table 3.2 A list of the conditions under which the sorbent was cycled for each method 56

Table 3.3 Elemental analysis results for the Al-containing sorbent series. 65

Table 3.4 BET surface area analysis of the Al-containing sorbents before and after calcination 67

CHAPTER 1

CAPTURING ANTHROPOGENIC CARBON DIOXIDE

1.1 The Carbon Dioxide Issue

Carbon dioxide has become a topic of great interest in recent years for its role as a greenhouse gas. The presence of CO_2 in the atmosphere has been linked to global warming, and some researchers claim that CO_2 is the single most important greenhouse gas for controlling the Earth's temperature.[1] The Earth System Research Laboratory (ESRL) in Mauna Loa, HI has been monitoring CO_2 levels since the 1950s (Figure 1.1). Their data clearly shows that, despite the seasonal fluctuations in the levels of CO_2 (red line), there has been a steady increase in atmospheric CO_2 from about 315 ppm in the 1950s to the present level of 390 ppm.[2]

The cause for this sharp increase in CO_2 over the past 60 years has been linked to anthropogenic sources. The Energy Information Administration (EIA), which is part of the U.S. Department of Energy (DOE), releases annual reports on US and global greenhouse gas emissions. In the latest report, the EIA estimated that the US released 6,576 million metric tons of CO_2 equivalents ($MMTCO_2e$) into the atmosphere in 2009. The estimate includes many greenhouse gases such as carbon dioxide, methane, and NOx gases. This actually represented a roughly 6% decrease in emissions from 2008, when 6,983 $MMTCO_2e$ were released. The decrease was attributed to the poor economy and a drop in the price of natural gas, which is a cleaner-burning energy source.[3]

The vast majority of US greenhouse gas emissions is in the form of carbon dioxide (Figure 1.2 A). Combustion of fossil fuels accounts for much of the CO_2

emitted; petroleum is the largest contributor accounting for 43% of emissions while coal is second accounting for 35%. The EIA also reports CO_2 emissions by sector which shows that 40% of emissions come from power generation alone (Figure 1.2 B).[3]

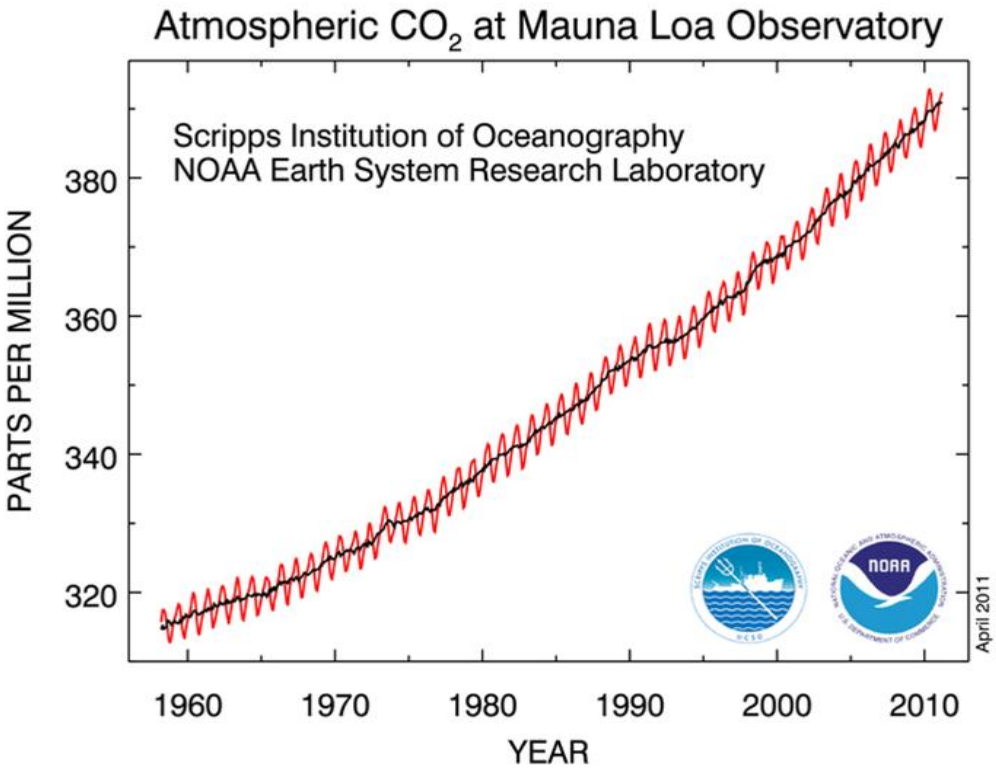

Figure 1.1 Seasonal trend (red line) and corrected average trend (black line) of atmospheric carbon dioxide over the past 60 years.[2]

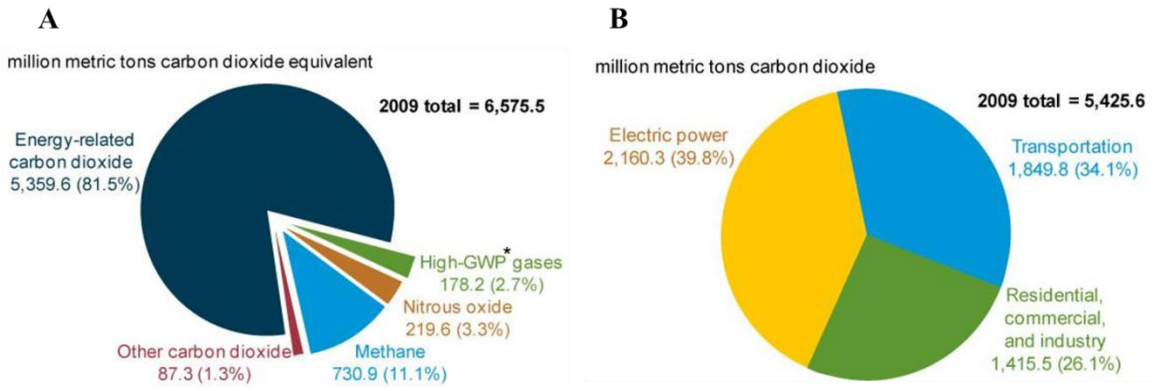

Figure 1.2 (A) Total US greenhouse gas emissions in 2009. **(B)** US carbon dioxide emissions by sector. *High-global warming potential gases.[3]

Globally, the US accounted for 20% of the world's total CO_2 output in 2007. While US and other Organization for Economic Cooperation and Development (OECD) members' emissions are not projected to increase drastically by 2035, emissions from other countries are expected to grow. China, for example, represented an estimated 21% of the roughly 30,000 MMT of CO_2 released worldwide in 2007. By 2035 it is estimated that China's output will have increased to 31% of worldwide CO_2 emissions, which are expected to grow to 42,000 MMT per year.[3]

The demand for power and the necessity to produce it cleanly will continue to grow as well. Wind power and solar power are very attractive renewable energy sources; however, they represent only a small fraction of power generation.[4, 5] To keep up with energy demands, countries are turning increasingly to coal. It has been predicted that the coal usage for power generation in the US, which is estimated to have roughly 30% of the world's coal reserves, will increase by 54% by 2030.[6, 7]

The increased reliance on coal comes at a time when Congress is beginning to consider incentives for reducing CO_2 emissions. Several plans have been proposed for reducing CO_2 emissions including a direct tax, an inflexible cap on emissions, and a cap-and-trade program.[8] Meanwhile, the DOE has established the goal of large-scale field testing of technology that can capture 90% of the CO_2 emitted from a power plant while raising the cost of electricity by no more than 20%.[7] The increasing demands for inexpensive electricity coupled with increasing government interest in CO_2 regulation has led to a large field of research aimed at CO_2 capture from coal-fired power plants.

1.2 The Integrated Gasification Combined Cycle

The integrated gasification combined cycle (IGCC) is one way by which energy from coal can be obtained cleanly. IGCC works by feeding a carbon source (coal) into a gasifier with a partially oxidizing atmosphere of oxygen and water vapor at temperatures exceeding 1000 °C (Figure 1.3). The resulting flue gas, which is composed mostly of CO and H_2, can be cleaned of particulates and sulfur-containing compounds.[9]

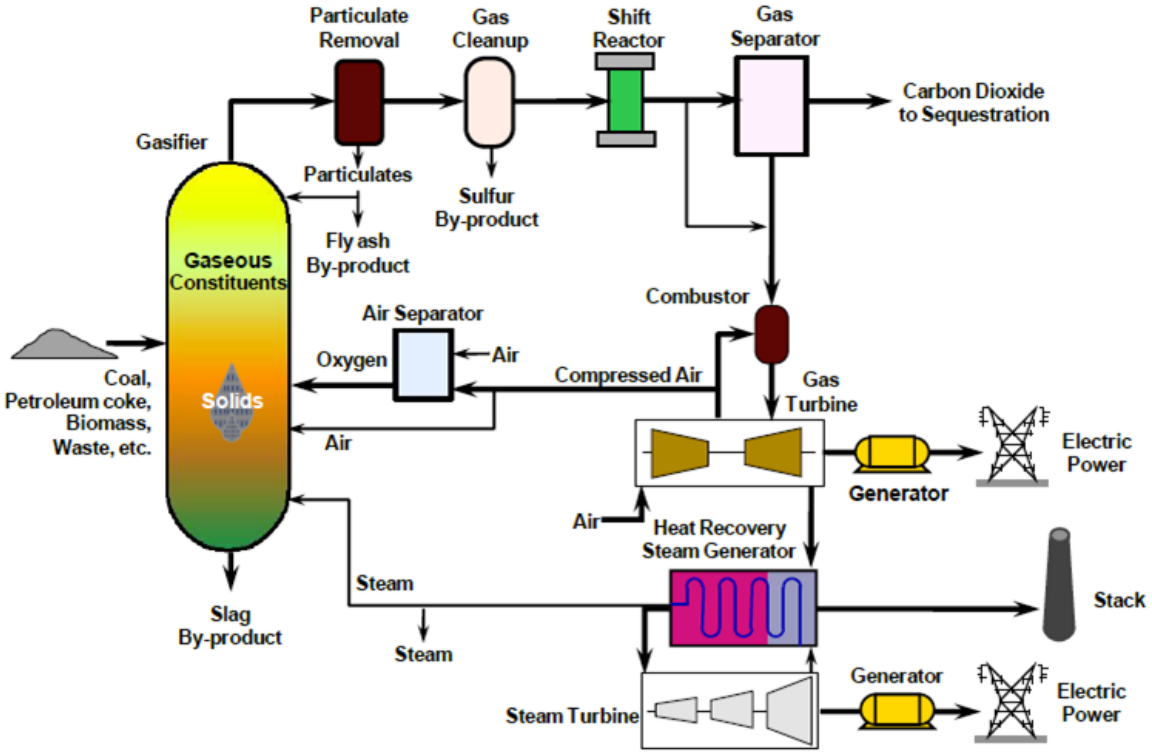

Figure 1.3 Diagram of the integrated gasification combined cycle with carbon dioxide capture.[9]

After cleaning, the flue gas undergoes the water-gas shift (WGS) reaction (Equation 1.1) at about 400°C to oxidize the CO and produce more H_2. Commercialized WGS reaction catalysts include Fe_2O_3-Cr_2O_3, CuO-ZnO-Al_2O_3, and Co-MoO_3-Al_2O_3;[10] however, noble metal catalysts such as Pt-OH_x species[11] and gold clusters[12] are currently being investigated for their catalytic properties. Additionally, work is being done to

eliminate the use of any catalysts by removing CO_2 from the WGS reactor, thereby shifting the reaction towards H_2 production.[13-15]

$$CO + H_2O \rightarrow CO_2 + H_2 \qquad \text{Eq. 1.1}$$

Finally, the H_2 can be separated from the CO_2 and used to generate electricity while the CO_2 is sequestered.[9] Plans for CO_2 sequestration involve injecting it underground where it can be stored for long periods of time without release into the atmosphere. Locations that have been considered are depleted oil and gas wells, deep coal seams, saline aquifers, ocean sediment, and basalts. The oil, gas, and coal locations are of particular interest because injection of CO_2 can dislodge previously unrecoverable resources from the porous rock.[16]

Currently, there are two IGCC plants operating in the US. The Wabash River plant was opened in 1995 in West Terre Haute, Indiana and is capable of producing 292 megawatts of electricity—262 megawatts of which supply the grid. The Polk Plant near Mulberry, Florida opened in 1997 with the capacity for producing 313 megawatts—250 megawatts of which go to the grid.[17] While both of these plants are extremely clean coal plants, neither is equipped with a gas separator unit for capturing carbon dioxide.

1.3 Sorbents for Carbon Dioxide Capture

There is a continuously growing need for new sorbents for efficient CO_2 capture. Many different classes of sorbents exist and several of those classes are described here.

This is not an exhaustive list, however, and more details on these sorbents as well as others can be found in recent review articles.[7, 18-21]

1.3.1 Amine-based Sorbents

Amine-based sorbents for CO_2 are an extremely well-studied field of research. Solutions of amines such as monoethanolamine (MEA), diethanolamine (DEA), or methyldiethanolamine (MDEA) in water have already been used for small-scale CO_2 capture.[22, 23]

The theoretical capacity of any amine-based sorbent is measured in terms of the number of moles of nitrogen available to react with CO_2. Under dry conditions where a base is not present, the maximum capacity is 0.5 mol CO_2 per mol N. When a base is present, however, the capacity doubles to 1.0 mol CO_2 per mol N.[24] The capacity is related to the mechanism for CO_2 capture with amines. For primary and secondary amines, the lone pair on the nitrogen atom attacks the partially positive carbon in CO_2 forming a zwitterionic species. A base (or in the case of no additional base, another nitrogen-containing molecule) then deprotonates the amine.[25, 26] In aqueous solutions containing tertiary amines, the lone pair on the nitrogen first attacks water forming a trialkyl ammonium and a hydroxide ion. The hydroxide reacts with CO_2 to form bicarbonate which is stabilized by the ammonium ion.[26, 27]

Various amines have been physically adsorbed onto silica supports for CO_2 capture. This is generally done by suspending silica in the amine with a volatile solvent. A synergistic effect has been observed between the silica and the amine where the combination of the two can adsorb more CO_2 than the bulk amine.[28] One example of a

well-studied amine impregnated on silica is poly(ethyleneimine) (PEI). This is an attractive polymer because it has up to 33% nitrogen by weight. The higher the nitrogen content of a sorbent, the higher its potential CO_2 capacity.[28-31]

The characteristics of amine impregnated silica sorbents depend largely on the pore structure of the silica and the type of amine. Soler-illa and coworkers showed that templated silica with ordered mesopores tends to adsorb more amine[32] while researchers working with Sayari[33] and Zhu[34] reported that silica with larger average pore diameters had higher equilibrium adsorption capacities for CO_2. Generally, it has been found that loading 50 wt% PEI onto a silica support captures the most CO_2. At loadings greater than 50 wt%, there is pore plugging due to the amine which limits the amount of CO_2 that can reach the interior of the support.[35] The type of amine dictates the degradation temperature of the sorbent. For PEI, the degradation temperature has been reported to be between 205 °C and 300°C.[28, 35]

Silica supported amines have moderate CO_2 adsorption capacities. Under dry conditions, Sayari and coworkers were able to capture 2.93 mmol CO_2/g sorbent which corresponded to an amine efficiency of 0.40 mol CO_2/mol N_2.[33] When water is introduced into the system, the capture capacity of amines should theoretically increase. The Song group showed that H_2O initially helps capture CO_2 during the first 30 min of carbonation. After 70 min, however, more water was adsorbed than CO_2 which suggests that water competitively binds with the amine, ultimately reducing capacity.[30, 31] The capacity is minimally affected by multiple adsorption/desorption cycles under dry conditions. Zhu and coworkers reported only a 4% loss in capacity over 7 cycles.[36]

Under wet conditions, however, the sorbent lost 50% of its capacity over just 4 cycles. This was attributed to amine leaching due to the presence of water.[37]

To minimize the effects of leaching due to water, amines have been covalently bonded to silica supports. Generally, aminoalkoxysilyl groups are reacted with silanol groups at the surface of the support.[38] The capacities of these sorbents under dry conditions depend largely on the type of amine bonded to the surface, however they are comparable to the wet-impregnated silica sorbents.[39-41] Under humid conditions, the covalently bound sorbents increased their CO_2 capacity by an average of 15%.[39, 41, 42] Recently, Sayari and Belmabkhout surveyed a series of anchored amine species on silica under both dry and humid conditions (Figure 1.4).[43] They found that after several cycles under dry conditions, the sorbents deactivated. In a humid atmosphere, however, the sorbents retained their capacity. The authors attributed the decay in capacity to the formation of stable urea species over multiple cycles. Water inhibits the formation of urea and instead promotes reversible bicarbonate formation thus preserving the capacity of each sorbent.

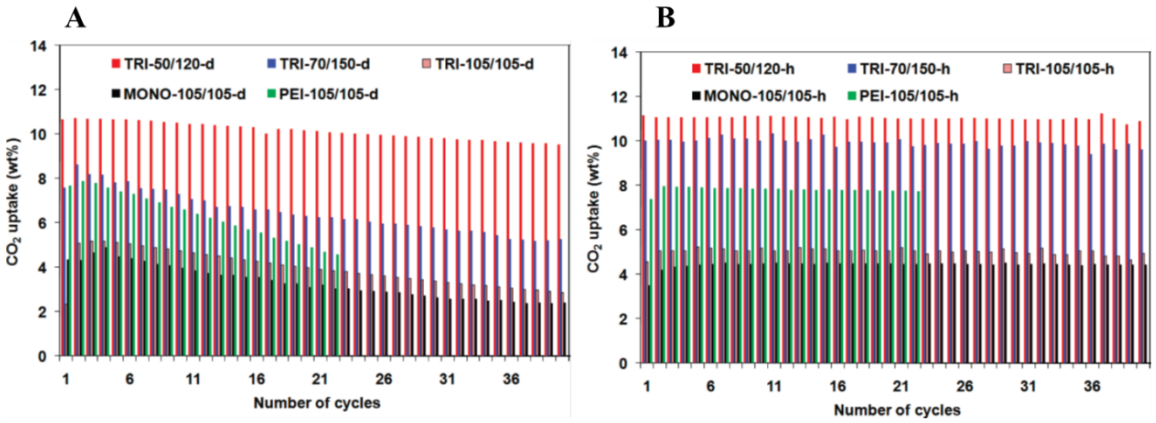

Figure 1.4 Data for six different anchored amine sorbents cycled under **(A)** dry conditions and **(B)** humid conditions (74% relative humidity at 25 °C).[43]

1.3.2 Zeolites

Zeolites are a class of porous aluminosilicates with varying Si:Al ratios. The lattice is constructed of AlO_4 and SiO_4 tetrahedra that create pores large enough for molecules to penetrate. The presence of aluminum in the lattice creates a net negative charge in the framework which must be balanced by cationic species. These cations are typically alkali metals that sit in the cavities of the zeolite. This can block pores and decrease pore volume causing the adsorption capacity of the zeolite for certain molecules to be reduced. The cations, however, also induce electric fields in the zeolite that can improve the adsorption of certain molecules such as CO_2.[18, 19, 44] Figure 1.5 shows the structure of faujasite (typical of synthetic X- and Y-type zeolites).[44] There are over 150 structures of zeolites known.[45]

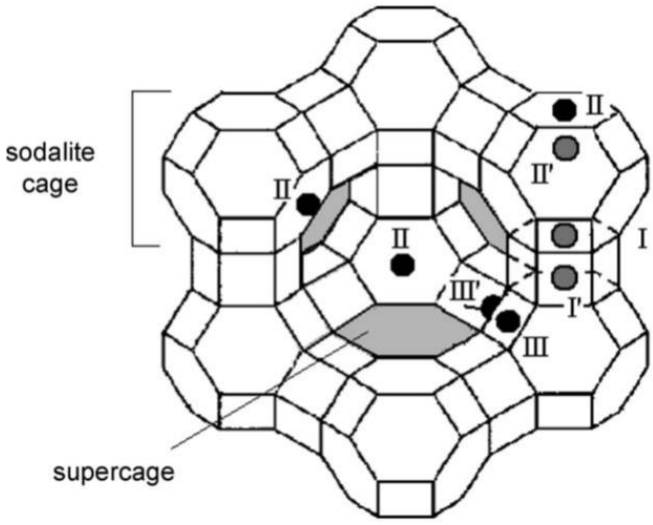

Figure 1.5 The structure of faujasite. The roman numerals indicate locations where cations typically reside.[44]

Zeolites are of interest because of the relatively low heats of adsorption for CO_2 (~60 kJ/mol).[46] This can ultimately save costs in sorbent regeneration but also means that zeolites can only capture CO_2 at low temperatures.[18] In general, CO_2 is physisorbed

to the zeolite, accounting for the low heat of adsorption. A slight reduction in capacity over several pressure swing adsorption (PSA) cycles can occur if some of the CO_2 chemisorbs to the zeolite. Siriwardane and coworkers showed, however, that by using temperature swing adsorption (TSA) and elevating the regeneration temperature to 350 °C, the sorbent can be fully regenerated.[47]

The CO_2 capacity of zeolites depends greatly on the temperature and pressure of adsorption. Generally, zeolites reach their highest capacities at high pressures and low temperatures. At 1 bar and 0 ºC, for example, many zeolites will absorb 1-5 mmol of CO_2 per gram of sorbent.[48-51] Work by Siriwardane showed that increasing the pressure above 1 bar does not significantly increase the amount of CO_2 adsorbed on zeolite 13X. Increasing the temperature from 30 °C to 120 ºC, however, significantly decreases the capacity of the sorbent at any given pressure (Figure 1.6).[46]

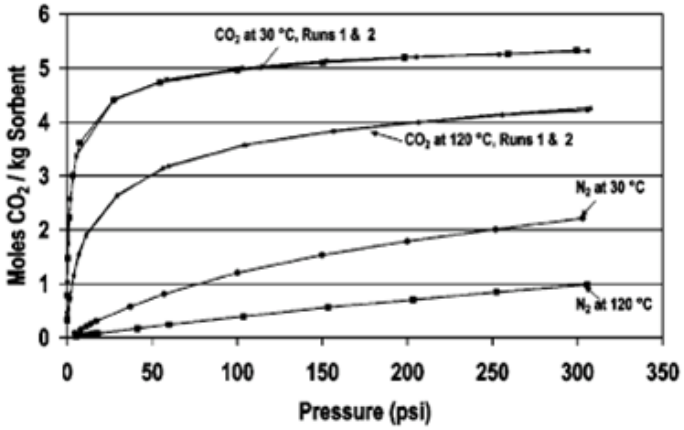

Figure 1.6 The effect of temperature on carbon dioxide and nitrogen adsorption curves on zeolite 13X.[46] 1 bar = 14.5 psi.

Research has been done to improve the adsorption capacity of various zeolite sorbents. Zhao and coworkers treated zeolite 13X with a kaolin binder and hydrothermally modified the sorbent in sodium hydroxide to obtain a 6.29 mmol/g

capacity at 0 °C and 1 bar.[52] Several researchers have shown that changing the Si:Al ratios and ion exchanging can improve capacity as well.[46, 53-55] Pawlesa and coworkers varied the Si:Al ratio on two zeolites, MCM-22 and MCM-49, between 15 and 40. [56] The group reported that lower Si:Al ratios improved the capacity of the zeolites (Figure 1.7). They also showed that in a comparison of Li^+, Na^+, K^+, and Cs^+, the Cs^+ exchanged sorbents performed the worst in all cases. These results agree with Siriwardane's work which showed that natural zeolites with high Na^+ content had higher capacities than sorbents with lower Na^+.[47]

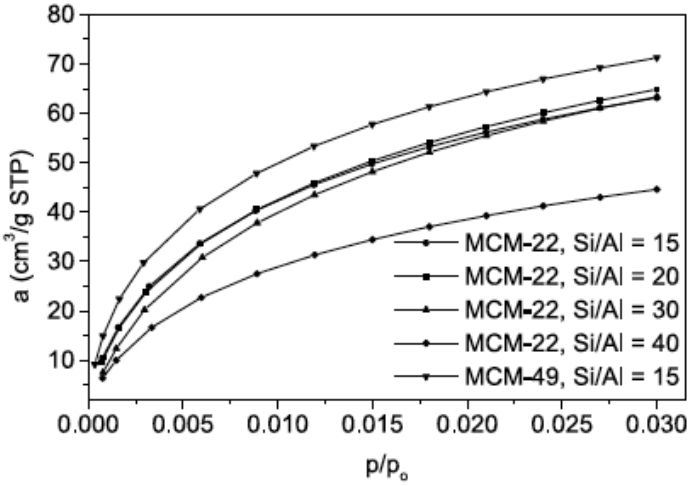

Figure 1.7 The effect of varying the Si:Al ratio in zeolites MCM-22 and MCM-49.[56]

Zeolites are attractive sorbents for CO_2 capture because many show preferential CO_2 adsorption over other gases. This is important for separating CO_2 from sources such as flue gas where a variety of gases are present.[57] Hernández-Huesca and coworkers studied the adsorption equilibria and kinetics of CO_2, CH_4, and N_2 on the natural zeolites ZAPS, ZNT, and ZN-19. They found that CO_2 and N_2 could diffuse into the pores of each zeolite making them effective sorbents for methane cleaning. Additionally, they noted that CO_2 capture was rapid and reached 70% of full capacity within 20 seconds.[58]

Researchers working with Goj showed in a competitive study between CO_2 and N_2 on zeolites ITQ-3 and ITQ-7, CO_2 is preferentially adsorbed over N_2.[59] By selecting the correct zeolite, one can efficiently remove CO_2 from a mixed gas stream. Another study showed that CO_2 is also preferentially adsorbed over ethane and ethene.[60]

The reason for high CO_2 selectivity in many zeolite sorbents has been attributed to the electric field of the zeolite. In a simulation by Goj and coworkers which considered only dispersion interactions between CO_2 or N_2 and ITQ zeolites, both gases filled the void volume in each material equally with no preference. When they considered Coulombic interactions, however, CO_2 adsorbed preferentially over N_2. This is due to the larger quadrupole moment of CO_2 interacting favorably with the electric field of the zeolite.[59] García-Sánchez and coworkers were later able to develop a force field through Monte Carlo simulations that accurately predicts the adsorption of CO_2 on various zeolites of different Si:Al ratios.[61]

In general, zeolites are negatively affected by the presence of water. Brandani and Ruthven showed that the CO_2 capacity on a number of cationic zeolite X adsorbents dropped rapidly as the percentage of preloaded water vapor was increased from 0-20%. They explained that the water affects the average interaction energy of the sorbent with CO_2.[62] An FTIR study by Gallei and Stumpf on CaY and NiY zeolites showed similar results.[63] Interestingly, it has been shown that small amounts of water can enhance CO_2 capture. Bertsch and Habgood showed that with 0.25 molecules of water per cavity on KX zeolites, CO_2 capture equilibrium was reached in a matter of seconds. In the absence of water, however, a pseudo-equilibrium was reached after 70 hrs. They suggest that the water increases the rate of chemisorption on the surface of the zeolite.[64] Rege and Yang

found similar results for zeolite 13X where they stated that trace amounts of water catalyzed the formation of bicarbonate species on the surface.[65]

Research into zeolite-based CO_2 sorbents is still very active.[46, 47] Recent work includes synthesizing membranes from zeolites,[66] creating sorbents from waste products like fly ash,[67] and modifying zeolite activation conditions such that natural zeolites can outperform synthetic ones.[68]

1.3.3 Activated carbons

Activated carbons (ACs) have many potential uses in, among other things, gas cleaning, water treatment, and catalysis.[69-71] The high surface area on ACs (usually greater than 500 m^2/g) makes them good candidates for CO_2 capture. They are attractive because of their rapid carbonation kinetics[72-74] and low desorption temperatures.[75] Additionally, ACs can be produced relatively inexpensively from a variety of materials such as wood, fly ash, resins, soybeans, and waste products such as carpet scraps.[76-78]

The performance of ACs is often compared to that of zeolites. Generally, it has been found that zeolites out-perform ACs at low pressures but at pressures greater than ~5 bar, ACs are superior.[76, 79-81] This phenomenon has been attributed to the porosity of the AC. At low pressures only the micropores smaller than 0.6 nm adsorb CO_2 whereas at higher pressures the entire micropore structure is used.[76] Both classes of sorbents, however, are very sensitive to changes in temperature. As temperature increases, the capacity of the sorbent rapidly decreases (Figure 1.8). Na and coworkers showed that over a small temperature range, between 15 and 55 °C, at 1 bar the capacity of an AC dropped from about 3.1 mmol/g to about 1.3 mmol/g.[73]

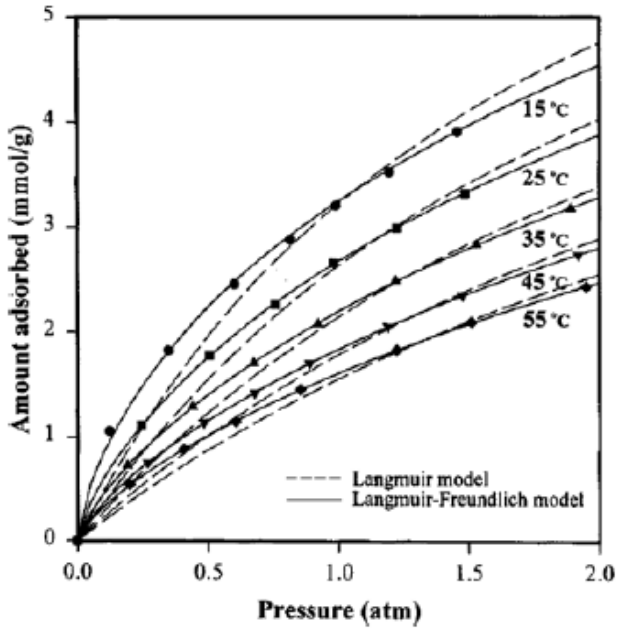

Figure 1.8 The effect of temperature at various pressures on the adsorption capacity of activated carbons.[73]

A significant amount of research, therefore, has been done to improve the CO_2 adsorption on ACs. This has been achieved by modifying the surface of ACs with nitrogen groups to increase the basicity of the sorbent.[82-88] Researchers working with Pevida treated the surface of two ACs with ammonia at various temperatures ranging from 200-800 °C. Ammonia treatment did not appear to have a large effect on the structure of the ACs at any temperature although the surface area generally decreased slightly. Temperature programed desorption (TPD) and X-ray photoelectron spectroscopy (XPS) showed that the nitrogen functionality on the AC depended on the temperature at which the AC was treated with ammonia. At temperatures above 600 °C, the nitrogen incorporated primarily into aromatic rings. At lower temperatures the nitrogen was found in functionalities such as amides, imides, imines, amines, and nitriles. Both ammonia-treated ACs showed the greatest improvement in CO_2 capture capacity at

25 °C when treated at 800 °C.[84] Bezerra and coworkers showed that avoiding heat treatment during surface modification of the AC allows the AC to maintain porosity and that the nitrogen functionalization improves the CO_2 capture capacity at elevated temperatures. A commercial AC was impregnated with amine groups from a solution of monoethanolamine at room temperature. The impregnated AC retained a very similar surface area to the parent AC. At room temperatures and pressures of CO_2 ranging from 0.1-10 bar, the parent AC significantly out-performed the amine-modified one. At 75 °C, however, the impregnated AC was superior to the parent.[82]

The CO_2 capture capacity of ACs has been observed to be negatively affected by water vapor.[89, 90] This is due to oxidation of the surface of the sorbent. Menéndez *et al.* showed that surface treatment conditions can drastically affect the stability of the AC towards water. A commercial AC was thermally treated at 950 °C in H_2 and in N_2. Both gases removed acidic oxygen-containing functionalities from the surface but only the H_2 treated sorbent was stable when exposed to water vapor. This was attributed to the fact that H_2 was more effective at oxygen removal and so the H_2-treated carbon surface was more resistant to attacks by water than the N_2-treated carbon surface.[91]

1.3.4 Metal Oxides

The basic sites on metal oxides make them attractive sorbents for CO_2, which is an acidic gas. Additionally, metal oxides can withstand high temperatures making them excellent candidates for incorporating CO_2 capture directly into a water-gas shift reactor.[14, 15] Despite the very high theoretical CO_2 capacities for many metal oxide

sorbents, they are not commercially used due to a rapid decay in performance over multiple carbonation/calcination cycles.[92, 93]

Of the metal oxides, CaO has emerged as the leading candidate for CO_2 capture. It has high capacity (up to 17.8 mmol CO_2 per gram of sorbent), operates at high temperature (>600 °C), and is very abundant and inexpensive. The Abanades group conducted a study on the cost of calcium oxide for capturing CO_2.[94, 95] They reported that it would cost US$ 0.0015 per mole of CO_2 captured with CaO. Compared to the cost of activated carbons ($ 0.25), zeolites ($ 0.20), and hydrotalcites ($ 4.00) per mole of CO_2, CaO is extremely inexpensive.

A detailed review of recent work done on calcium oxides will be presented in Chapter 3. Other metal oxides that have received attention recently include Oxides of magnesium,[96] aluminum,[97] chromium,[98] copper,[99] tantalum,[100] iron,[101] barium,[102] cesium,[103] rubidium,[104] potassium,[105] sodium,[106] and lithium.[107]

1.3.5 Lithium Zirconates

Lithium zirconate sorbents are a class of materials that have been studied recently for their high temperature CO_2 adsorption properties. The reversible reaction of lithium zirconate with CO_2 is shown in Equation 1.2. Although the reverse reaction of lithium carbonate with zirconia has been known for some time, the reaction of lithium zirconate with carbon dioxide has been studied only within the past 15 years, when Nakagawa and Ohashi reported capturing 76.3% of the maximum capacity.[108]

$$Li_2ZrO_3 + CO_2 \rightleftharpoons Li_2CO_3 + ZrO_2 \qquad \text{Eq. 1.2}$$

Lithium zirconates are attractive because they are stable over multiple carbonation/calcination cycles and have a relatively high theoretical capacity of 28 wt% CO_2 or 4.5 mmol/g. Additionally, they operate at relatively high temperatures ranging from 400-750 °C. Presently, however, they exhibit very slow kinetics due to the formation of a Li_2CO_3 shell (Figure 1.9 A) making them impractical for industrial use.[109-113] Consequently, work on this class of sorbents has focused on improving the rate of carbonation.

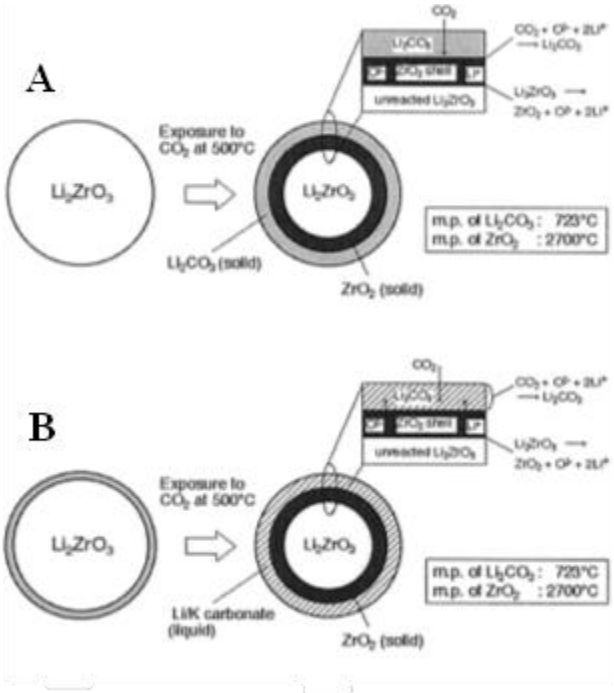

Figure 1.9 (A) Mechanism of the formation of a lithium carbonate shell around pure lithium zirconate. **(B)** Formation of a molten lithium carbonate shell upon the addition of potassium allowing faster diffusion to the particle center.[114]

Ida and Lin showed that by doping the Li_2ZrO_3 with potassium carbonate, the sorption rate was increased by a factor of 40 at 500 °C. They proposed a double-shell mechanism to explain this phenomenon (Figure 1.9 B) where adding potassium to the sorbent caused a lithium/potassium carbonate eutectic to be formed. This mixture melts at 500 °C which allows for faster diffusion of Li^+ ions and CO_2 through the liquid

eutectic shell than the solid Li_2CO_3 shell. The rate of desorption, however, was not enhanced by adding potassium because the desorption temperature (780 °C) was above the melting point of Li_2CO_3.[114]

Sodium has also been used to improve the sorption kinetics of lithium zirconates. Doping the sorbent with sodium is advantageous because it forms sodium zirconate (Na_2ZrO_3), which is an active sorbent in the same temperature ranges that lithium zirconates are.[111] Pfeiffer and coworkers found that a 1:1 mole ratio of Li:Na yields an adsorption rate 4 times faster than either the lithium or the sodium zirconate by itself. After 270 min. the 1:1 Li:Na sorbent captured 75.3 % (0.196 $g_{CO2}/g_{LiNaZrO3}$) of its maximum capacity.[115, 116]

It has been shown that the crystal structure of the lithium zirconate has a large impact on the kinetics of the sorbent. Generally, two or three phases are discussed with carbon dioxide adsorption: the monoclinic phase (m-$Li_6Zr_2O_7$), the tetragonal phase (t-Li_2ZrO_3), and occasionally the triclinic phase. The monoclinic phase is argued to have the highest capacity due to higher lithium content.[109, 112] Yin and coworkers synthesized m-$Li_6Zr_2O_7$ and demonstrated it out-performed t-Li_2ZrO_3 at lower partial pressures of CO_2. Interestingly, they found that after the first cycle the sorbent regenerated to the triclinic phase above 900 °C, which could be recycled multiple times.[112] Other work, however, suggests that forming the triclinic structure prevents the sorbent from regenerating.[117] The tetragonal phase, however, has been found to have the fastest kinetics.[112, 118-121] Ochoa-Fernández and coworkers were able to synthesize t-Li_2ZrO_3 spherical agglomerates of nanocrystals by spray pyrolysis. The sorbent reached 96% of full capacity within 5 min. at 575 °C under CO_2. They fully regenerated the sorbent at

650 °C which minimized adverse effects due to thermal shock. The sorbent maintained capacity over multiple cycles.[120]

Research on alkali metal oxides is not limited to only those containing lithium. Other alkali metal salts have been investigated including Na_2CO_3[122] and K_2CO_3.[123, 124]

1.3.6 Hydrotalcites

Hydrotalcites are of the general formula $[M^{2+}_{1-x}M^{3+}_{x}(OH)_2]^{x+}\bullet[A^{m-}_{x/m}\bullet nH_2O]^{x-}$. The positively charged brucite-like layers $[M^{2+}_{1-x}M^{3+}_{x}(OH)_2]^{x+}$ contain M^{3+} cations (Al^{3+}, Fe^{3+}, Cr^{3+}) which substitute for some of the M^{2+} cations (Mg^{2+}, Ni^{2+}, Zn^{2+}, Cu^{2+}, Mn^{2+}). Water and interlayer anions A^{m-} (CO_3^{2-}, SO_4^{2-}, NO_3^-, Cl^-, OH^-) offset the positive charge. Typical values of x range from 0.17 to 0.33.[125]

These materials are attractive CO_2 sorbents for their application in realistic carbonation conditions. Sorbents must retain high CO_2 capacity when flue gas, which has high water content, is passed over them. Unlike activated carbons which perform very poorly in the presence of water,[89, 90] hydrotalcites can capture more CO_2 in wet conditions than they can in dry conditions (Figure 1.10).[72, 126] Reddy and coworkers prepared an amorphous layered double oxide (LDO) by heating a Mg-Al-CO_3 layered double hydroxide (LDH) to 400 °C. They found that the under dry conditions the sorbent captured 0.61 mmol CO_2/g sorbent while the same sorbent exposed to wet conditions captured 0.71 mmol/g. Although the presence of water vapor did not increase the kinetics of adsorption, the total capacity was increased.[127]

The layered structure of Mg-Al-CO_3 hydrotalcites is sensitive to temperature. Hutson and coworkers reported that heating the hydrotalcite to 200 °C removes the

interlayer water and causes the interlayer spacing to decrease by 0.6 Å.[128] At this temperature, roughly half of the CO_2 captured is chemisorbed due to the exposed Mg^{2+} cations. Upon further heating to 400 °C, however, only about 18% of the CO_2 is chemisorbed. At 400 °C, the interlayer decomposes and fully dehydrates leaving an amorphous 3-D structure. The surface area and pore volume available for physisorption increase while the availability of the Mg^{2+} cation decreases.

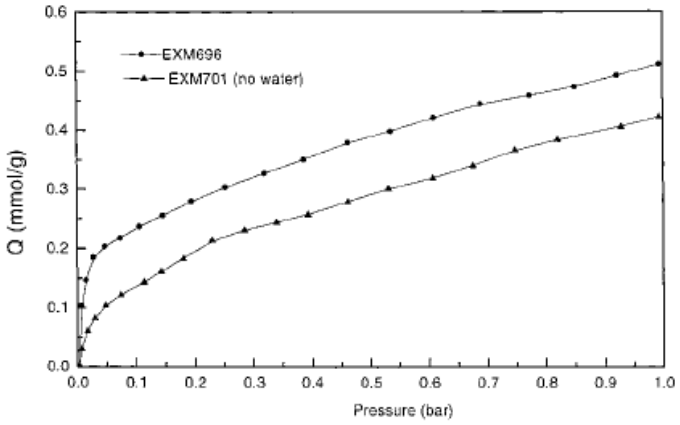

Figure 1.10 The effect of the presence of water on the capture capacity of a hydrotalcite.[129]

Adding dopants to the hydrotalcites, such as cesium and potassium, can improve sorbent stability over multiple cycles. Oliveira and coworkers impregnated several commercial hydrotalcites with either cesium or potassium. They found that the commercial MG30 hydrotalcite impregnated with 20 wt% potassium not only had the highest capacity at 0.76 mmol CO_2/g sorbent but also lost only 7% of its initial capacity over 75 cycles.[130] The high capacity is crucial for the continued investigation into hydrotalcites. Although the capacity of hydrotalcites can be tailored by optimizing the aluminum content and the heat treatment temperature, the maximum capacity for CO_2 of most hydrotalcites is still below 1 mmol CO_2/g sorbent.[129]

1.3.7 Metal-Organic Frameworks

Metal-organic frameworks (MOFs) are a relatively new class of materials with extremely high surface areas. MOF-5 was first reported by the Yaghi group to have a Brunauer-Emmett-Teller (BET) surface area of 2900 m^2/g.[131] Yaghi and coworkers subsequently reported the ability to tailor the pore spaces of the MOFs according to the different ligands used during synthesis.[132] They tested IRMOF-6 with methane and found the MOF to have an extremely high methane capacity.

This work led several researchers to test many different MOFs for their CO_2 capacities.[133-137] The CO_2 capture capacity of any particular MOF has been shown to be pressure dependent. At high pressures of around 40 atm, MOF-177 captured 33.5 mmol CO_2/g sorbent (Figure 1.11).[135]

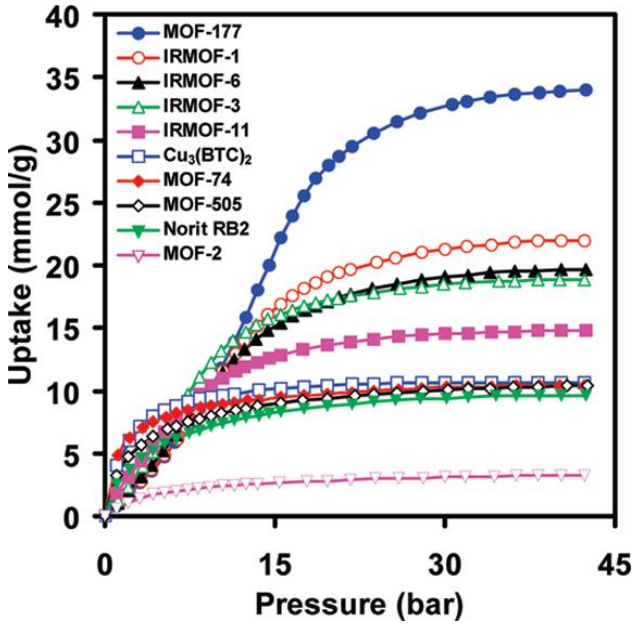

Figure 1.11 The carbon dioxide capture capacity of various MOFs as a function of pressure.[135]

MOFs are currently showing promise as high capacity CO_2 sorbents. However, research on this class of sorbents is still in its infancy. Regenerability, competitive gases,

and low CO_2 concentration tests all still need to be performed and reported.[18] The results of these experiments in the upcoming years will determine the role MOFs will play in controlling anthropogenic CO_2 emissions.

1.4 Summary

Carbon dioxide is the most environmentally impactful greenhouse gas. Despite the rapidly increasing level of CO_2 in the atmosphere, global anthropogenic CO_2 emissions are projected to increase. Because a large percentage of CO_2 emissions come from power generation (40% of emissions in the US), much research has focused on designing inexpensive technology to capture CO_2 and other pollutants from power plants. Although there are many classes of CO_2 sorbents, none of them are currently being used to capture the gas from power plants. Low temperature sorbents (zeolites, ACs, MOFs) are advantageous because they generally require very little energy (and thus low cost) to regenerate. However, these sorbents do not adequately capture CO_2 at high temperatures (>500 °C); consequently there is an energy cost for cooling gas streams down for CO_2 capture and then heating them again for energy generation. High temperature sorbents (lithium zirconates, hydrotalcites, metal oxides) solve this issue, however many of these sorbents exhibit poor cyclic stability or slow kinetics. The field of designing sorbents for CO_2 capture is an active one, and will continue to receive much attention as long as atmospheric CO_2 levels remain high.

1.5 References

1. Lacis, A. A.; Schmidt, G. A.; Rind, D.; Ruedy, R. A. Atmospheric CO2: Principal Control Knob Governing Earth's Temperature. *Science* **2010,** *330,* 356-359.

2. Tans, P.; Keeling, R. http://www.esrl.noaa.gov/gmd/ccgg/trends/ (accessed April 16, 2011).

3. *Emissions of Greenhouse Gases in the United States*; U.S. Energy Information Administration: 2011.

4. Parida, B.; Iniyan, S.; Goic, R. A review of solar photovoltaic technologies. *Renew. Sust. Energ. Rev.* **2011,** *15*, 1625-1636.

5. Kaldellis, J. K.; Zafirakis, D. The wind energy (r)evolution: A short review of a long history. *Renew. Energy* **2011,** *36*, 1887-1901.

6. Hook, M.; Aleklett, K. Historical trends in American coal production and a possible future outlook. *Int. J. Coal Geol.* **2009,** *78*, 201-216.

7. Figueroa, J. D.; Fout, T.; Plasynski, S.; McIlvried, H.; Srivastava, R. D. Advances in CO2 capture technology - The US Department of Energy's Carbon Sequestration Program. *Int. J. Greenh. Gas Control* **2008,** *2*, 9-20.

8. *Policy Options for Reducing CO_2 Emissions*; Congressional Budget Office: 2008.

9. Breault, R. W. Gasification Processes Old and New: A Basic Review of the Major Technologies. *Energies* **2010,** *3*, 216-240.

10. Liu, Q. S.; Zhang, Q. C.; Ma, W. P.; He, R. X.; Kou, L. J.; Mou, Z. J. Progress in water-gas-shift catalysts. *Prog. Chem.* **2005,** *17*, 389-398.

11. Zhai, Y.; Pierre, D.; Si, R.; Deng, W.; Ferrin, P.; Nilekar, A. U.; Peng, G.; Herron, J. A.; Bell, D. C.; Saltsburg, H.; Mavrikakis, M.; Flytzani-Stephanopoulos, M. Alkali-Stabilized Pt-OHx Species Catalyze Low-Temperature Water-Gas Shift Reactions. *Science* **2010,** *329*, 1633-1636.

12. Williams, W. D.; Shekhar, M.; Lee, W.-S.; Kispersky, V.; Delgass, W. N.; Ribeiro, F. H.; Kim, S. M.; Stach, E. A.; Miller, J. T.; Allard, L. F. Metallic Corner Atoms in Gold Clusters Supported on Rutile Are the Dominant Active Site during Water-Gas Shift Catalysis. *J. Am. Chem. Soc.* **2010,** *132*, 14018-14020.

13. Ramkumar, S.; Fan, L. S. Calcium Looping Process (CLP) for Enhanced Noncatalytic Hydrogen Production with integrated Carbon Dioxide Capture. *Energ. Fuel.* **2010,** *24*, 4408-4418.

14. Ortiz, A. L.; Harrison, D. P. Hydrogen production using sorption-enhanced reaction. *Ind. Eng. Chem. Res.* **2001,** *40*, 5102-5109.

15. Wu, C. F.; Williams, P. T. A novel Ni-Mg-Al-CaO catalyst with the dual functions of catalysis and CO2 sorption for H-2 production from the pyrolysis-gasification of polypropylene. *Fuel* **2010,** *89*, 1435-1441.

16. Seto, C. J.; McRae, G. J. Reducing Risk in Basin Scale CO2 Sequestration: A Framework for Integrated Monitoring Design. *Environ. Sci. Technol.* **2011,** *45*, 845-859.

17. Pioneering Gasification Plants. http://www.fossil.energy.gov/programs/powersystems/gasification/gasificationpioneer.html (accessed April 17, 2011).

18. Choi, S.; Drese, J. H.; Jones, C. W. Adsorbent Materials for Carbon Dioxide Capture from Large Anthropogenic Point Sources. *ChemSusChem* **2009,** *2*, 796-854.

19. Wang, Q. A.; Luo, J. Z.; Zhong, Z. Y.; Borgna, A. CO2 capture by solid adsorbents and their applications: current status and new trends. *Energy Environ. Sci.* **2011,** *4*, 42-55.

20. Hao, G.-P.; Li, W.-C.; Lu, A.-H. Novel porous solids for carbon dioxide capture. *J. Mater. Chem.* **2011,** *21*, 6447-6451.

21. Yong, Z.; Mata, V.; Rodrigues, A. E. Adsorption of carbon dioxide at high temperature - a review. *Sep. Purif. Technol.* **2002,** *26*, 195-205.

22. Danckwerts, P. V. Reaction of CO2 with ethanolamines. *Chem. Eng. Sci.* **1979,** *34*, 443-446.

23. Versteeg, G. F.; Van Dijck, L. A. J.; Van Swaaij, W. P. M. On the kinetics between CO2 and alkanolamines both in aqueous and non-aqueous solutions. An overview. *Chem. Eng. Commun.* **1996,** *144*, 113-158.

24. Sartori, G.; Savage, D. W. Sterically hindered amines for CO2 removal from gases. *Ind. Eng. Chem. Fund.* **1983,** *22*, 239-249.

25. Caplow, M. Kinetics of carbamate formation and breakdown. *J. Am. Chem. Soc.* **1968,** *90*, 6795-6803.

26. Vaidya, P. D.; Kenig, E. Y. CO2-alkanolamine reaction kinetics: A review of recent studies. *Chem. Eng. Technol.* **2007,** *30*, 1467-1474.

27. Donaldson, T. L.; Nguyen, Y. N. Carbon-dioxide reaction-kinetics and transport in aqueous amine membranes. *Ind. Eng. Chem. Fund.* **1980,** *19*, 260-266.

28. Xu, X. C.; Song, C. S.; Andresen, J. M.; Miller, B. G.; Scaroni, A. W. Novel polyethylenimine-modified mesoporous molecular sieve of MCM-41 type as high-capacity adsorbent for CO2 capture. *Energ. Fuel.* **2002,** *16*, 1463-1469.

29. Xu, X. C.; Song, C. S.; Andresen, J. M.; Miller, B. G.; Scaroni, A. W. Preparation and characterization of novel CO2 "molecular basket" adsorbents based on polymer-modified mesoporous molecular sieve MCM-41. *Microporous Mesoporous Mat.* **2003,** *62*, 29-45.

30. Xu, X. C.; Song, C. S.; Miller, B. G.; Scaroni, A. W. Adsorption separation of carbon dioxide from flue gas of natural gas-fired boiler by a novel nanoporous "molecular basket" adsorbent. *Fuel Process. Technol.* **2005,** *86*, 1457-1472.

31. Xu, X. C.; Song, C. S.; Miller, B. G.; Scaroni, A. W. Influence of moisture on CO2 separation from gas mixture by a nanoporous adsorbent based on polyethylenimine-modified molecular sieve MCM-41. *Ind. Eng. Chem. Res.* **2005,** *44*, 8113-8119.

32. Soler-illia, G. J. D.; Sanchez, C.; Lebeau, B.; Patarin, J. Chemical strategies to design textured materials: From microporous and mesoporous oxides to nanonetworks and hierarchical structures. *Chem. Rev.* **2002,** *102*, 4093-4138.

33. Franchi, R. S.; Harlick, P. J. E.; Sayari, A. Applications of pore-expanded mesoporous silica. 2. Development of a high-capacity, water-tolerant adsorbent for CO2. *Ind. Eng. Chem. Res.* **2005,** *44*, 8007-8013.

34. Yue, M. B.; Sun, L. B.; Cao, Y.; Wang, Y.; Wang, Z. J.; Zhu, J. H. Efficient CO2 capturer derived from as-synthesized MCM-41 modified with amine. *Chem.-Eur. J.* **2008,** *14*, 3442-3451.

35. Son, W. J.; Choi, J. S.; Ahn, W. S. Adsorptive removal of carbon dioxide using polyethyleneimine-loaded mesoporous silica materials. *Microporous Mesoporous Mat.* **2008,** *113*, 31-40.

36. Yue, M. B.; Chun, Y.; Cao, Y.; Dong, X.; Zhu, J. H. CO2 capture by As-prepared SBA-15 with an occluded organic template. *Adv. Funct. Mater.* **2006,** *16*, 1717-1722.

37. Hicks, J. C.; Drese, J. H.; Fauth, D. J.; Gray, M. L.; Qi, G. G.; Jones, C. W. Designing adsorbents for CO2 capture from flue gas-hyperbranched aminosilicas capable,of capturing CO2 reversibly. *J. Am. Chem. Soc.* **2008,** *130*, 2902-2903.

38. Brinker, C. J.; Scherer, G. W., *Sol-Gel Science: The Physics and Chemistry of Sol-Gel Processing*. Academic Press, Inc.: San Diego, 1990.

39. Harlick, P. J. E.; Sayari, A. Applications of pore-expanded mesoporous silica. 5. Triamine grafted material with exceptional CO2 dynamic and equilibrium adsorption performance. *Ind. Eng. Chem. Res.* **2007,** *46*, 446-458.

40. Hiyoshi, N.; Yogo, K.; Yashima, T. Adsorption of carbon dioxide on amine modified SBA-15 in the presence of water vapor. *Chem. Lett.* **2004,** *33*, 510-511.

41. Serna-Guerrero, R.; Da'na, E.; Sayari, A. New Insights into the Interactions of CO2 with Amine-Functionalized Silica. *Ind. Eng. Chem. Res.* **2008,** *47*, 9406-9412.

42. Tsuda, T.; Fujiwara, T.; Taketani, Y.; Saegusa, T. Amino silica-gels acting as a carbon-dioxide absorbent. *Chem. Lett.* **1992,** *21*, 2161-2164.

43. Sayari, A.; Belmabkhout, Y. Stabilization of Amine-Containing CO2 Adsorbents: Dramatic Effect of Water Vapor. *J. Am. Chem. Soc.* **2010,** *132*, 6312-6314.

44. Walton, K. S.; Abney, M. B.; LeVan, M. D. CO2 adsorption in Y and X zeolites modified by alkali metal cation exchange. *Microporous Mesoporous Mat.* **2006,** *91*, 78-84.

45. Baerlocher, C.; McCusker, L. B. Database of Zeolite Structures. http://www.iza-structure.org/databases/.

46. Siriwardane, R. V.; Shen, M. S.; Fisher, E. P. Adsorption of CO2 on zeolites at moderate temperatures. *Energ. Fuel.* **2005,** *19*, 1153-1159.

47. Siriwardane, R. V.; Shen, M. S.; Fisher, E. P. Adsorption of CO2, N-2, and O-2 on natural zeolites. *Energ. Fuel.* **2003,** *17*, 571-576.

48. Harlick, P. J. E.; Tezel, F. H. An experimental adsorbent screening study for CO2 removal from N-2. *Microporous Mesoporous Mat.* **2004,** *76*, 71-79.

49. Shao, W.; Zhang, L. Z.; Li, L. X.; Lee, R. L. Adsorption of CO2 and N-2 on synthesized NaY zeolite at high temperatures. *Adsorpt.-J. Int. Adsorpt. Soc.* **2009,** *15*, 497-505.

50. Wang, Y.; Levan, M. D. Adsorption Equilibrium of Carbon Dioxide and Water Vapor on Zeolites 5A and 13X and Silica Gel: Pure Components. *J. Chem. Eng. Data* **2009,** *54*, 2839-2844.

51. Zukal, A.; Dominguez, I.; Mayerova, J.; Cejka, J. Functionalization of Delaminated Zeolite ITQ-6 for the Adsorption of Carbon Dioxide. *Langmuir* **2009,** *25*, 10314-10321.

52. Zhao, Z. L.; Cui, X. Y.; Ma, J. H.; Li, R. F. Adsorption of carbon dioxide on alkali-modified zeolite 13X adsorbents. *Int. J. Greenh. Gas Control* **2007,** *1*, 355-359.

53. Armandi, M.; Garrone, E.; Arean, C. O.; Bonelli, B. Thermodynamics of Carbon Dioxide Asdorption on the Protonic Zeolite H-ZSM-5. *ChemPhysChem* **2009,** *10*, 3316-3319.

54. Bulanek, R.; Frolich, K.; Frydova, E.; Cicmanec, P. Microcalorimetric and FTIR Study of the Adsorption of Carbon Dioxide on Alkali-Metal Exchanged FER Zeolites. *Top. Catal.* **2010,** *53*, 1349-1360.

55. Galhotra, P.; Navea, J. G.; Larsen, S. C.; Grassian, V. H. Carbon dioxide ((CO2)-O-16 and (CO2)-O-18) adsorption in zeolite Y materials: effect of cation, adsorbed water and particle size. *Energy Environ. Sci.* **2009,** *2*, 401-409.

56. Pawlesa, J.; Zukal, A.; Cejka, J. Synthesis and adsorption investigations of zeolites MCM-22 and MCM-49 modified by alkali metal cations. *Adsorpt.-J. Int. Adsorpt. Soc.* **2007,** *13*, 257-265.

57. Cavenati, S.; Grande, C. A.; Rodrigues, A. E. Adsorption equilibrium of methane, carbon dioxide, and nitrogen on zeolite 13X at high pressures. *J. Chem. Eng. Data* **2004,** *49*, 1095-1101.

58. Hernandez-Huesca, R.; Diaz, L.; Aguilar-Armenta, G. Adsorption equilibria and kinetics of CO2, CH4 and N-2 in natural zeolites. *Sep. Purif. Technol.* **1999,** *15*, 163-173.

59. Goj, A.; Sholl, D. S.; Akten, E. D.; Kohen, D. Atomistic simulations of CO2 and N-2 adsorption in silica zeolites: The impact of pore size and shape. *J. Phys. Chem. B* **2002,** *106*, 8367-8375.

60. Romero-Perez, A.; Aguilar-Armenta, G. Adsorption Kinetics and Equilibria of Carbon Dioxide, Ethylene, and Ethane on 4A(CECA) Zeolite. *J. Chem. Eng. Data* **2010,** *55*, 3625-3630.

61. Garcia-Sanchez, A.; Ania, C. O.; Parra, J. B.; Dubbeldam, D.; Vlugt, T. J. H.; Krishna, R.; Calero, S. Transferable Force Field for Carbon Dioxide Adsorption in Zeolites. *J. Phys. Chem. C* **2009,** *113*, 8814-8820.

62. Brandani, F.; Ruthven, D. M. The effect of water on the adsorption of CO2 and C3H8 on type X zeolites. *Ind. Eng. Chem. Res.* **2004,** *43*, 8339-8344.

63. Gallei, E.; Stumpf, G. Infrared spectroscopic studies of adsorption of carbon-dioxide and coadsorption of carbon-dioxide and water on CaY-zeolites and NiY-zeolites. *J. Colloid Interface Sci.* **1976,** *55*, 415-420.

64. Bertsch, L.; Habgood, H. W. An infrared spectroscopic study of adsorption of water and carbon dioxide by linde milecular sieve X. *J. Phys. Chem.* **1963,** *67*, 1621-1628.

65. Rege, S. U.; Yang, R. T. A novel FTIR method for studying mixed gas adsorption at low concentrations: H2O and CO2 on NaX zeolite and gamma-alumina. *Chem. Eng. Sci.* **2001,** *56*, 3781-3796.

66. White, J. C.; Dutta, P. K.; Shqau, K.; Verweij, H. Synthesis of Ultrathin Zeolite Y Membranes and their Application for Separation of Carbon Dioxide and Nitrogen Gases. *Langmuir* **2010,** *26*, 10287-10293.

67. Lee, K. M.; Jo, Y. M. Synthesis of zeolite from waste fly ash for adsorption of CO2. *J. Mater. Cycles Waste Manag.* **2010,** *12*, 212-219.

68. Alonso-Vicario, A.; Ochoa-Gomez, J. R.; Gil-Rio, S.; Gomez-Jimenez-Aberasturi, O.; Ramirez-Lopez, C. A.; Torrecilla-Soria, J.; Dominguez, A. Purification and upgrading of biogas by pressure swing adsorption on synthetic and natural zeolites. *Microporous Mesoporous Mat.* **2010,** *134*, 100-107.

69. Atkinson, J. D.; Fortunato, M. E.; Dastgheib, S. A.; Rostam-Abadi, M.; Rood, M. J.; Suslick, K. S. Synthesis and characterization of iron-impregnated porous carbon spheres prepared by ultrasonic spray pyrolysis. *Carbon* **2011,** *49*, 587-598.

70. Fortunato, M. E.; Rostam-Abadi, M.; Suslick, K. S. Nanostructured Carbons Prepared by Ultrasonic Spray Pyrolysis. *Chem. Mat.* **2010,** *22*, 1610-1612.

71. Skrabalak, S. E.; Suslick, K. S. Porous Carbon Powders Prepared by Ultrasonic Spray Pyrolysis. *J. Am. Chem. Soc.* **2006,** *128*, 12642-12643.

72. Do, D. D.; Wang, K. A new model for the description of adsorption kinetics in heterogeneous activated carbon. *Carbon* **1998,** *36*, 1539-1554.

73. Na, B. K.; Koo, K. K.; Eum, H. M.; Lee, H.; Song, H. K. CO2 recovery from flue gas by PSA process using activated carbon. *Korean J. Chem. Eng.* **2001,** *18*, 220-227.

74. Sircar, S. Sorption of carbon-dioxide on activated carbons-effect of the heat of sorption during kinetic measurements. *Carbon* **1981,** *19*, 153-160.

75. Sircar, S.; Golden, T. C.; Rao, M. B. Activated carbon for gas separation and storage. *Carbon* **1996,** *34*, 1-12.

76. Martin, C. F.; Plaza, M. G.; Pis, J. J.; Rubiera, F.; Pevida, C.; Centeno, T. A. On the limits of CO2 capture capacity of carbons. *Sep. Purif. Technol.* **2010,** *74*, 225-229.

77. Olivares-Marin, M.; Maroto-Valer, M. M. Preparation of a highly microporous carbon from a carpet material and its application as CO2 sorbent. *Fuel Process. Technol.* **2011,** *92*, 322-329.

78. Thote, J. A.; Iyer, K. S.; Chatti, R.; Labhsetwar, N. K.; Biniwale, R. B.; Rayalu, S. S. In situ nitrogen enriched carbon for carbon dioxide capture. *Carbon* **2010,** *48*, 396-402.

79. Chue, K. T.; Kim, J. N.; Yoo, Y. J.; Cho, S. H.; Yang, R. T. Comparison of activated carbon and zeolite 13X for CO2 recovery from flue-gas by pressure swing adsorption. *Ind. Eng. Chem. Res.* **1995,** *34*, 591-598.

80. Siriwardane, R. V.; Shen, M. S.; Fisher, E. P.; Poston, J. A. Adsorption of CO2 on molecular sieves and activated carbon. *Energ. Fuel.* **2001,** *15*, 279-284.

81. Drage, T. C.; Blackman, J. M.; Pevida, C.; Snape, C. E. Evaluation of Activated Carbon Adsorbents for CO2 Capture in Gasification. *Energ. Fuel.* **2009,** *23*, 2790-2796.

82. Bezerra, D. P.; Oliveira, R. S.; Vieira, R. S.; Cavalcante, C. L.; Azevedo, D. C. S. Adsorption of CO2 on nitrogen-enriched activated carbon and zeolite 13X. *Adsorpt.-J. Int. Adsorpt. Soc.* **2011,** *17*, 235-246.

83. Hao, G. P.; Li, W. C.; Qian, D.; Lu, A. H. Rapid Synthesis of Nitrogen-Doped Porous Carbon Monolith for CO2 Capture. *Adv. Mater.* **2010,** *22*, 853-857.

84. Pevida, C.; Plaza, M. G.; Arias, B.; Fermoso, J.; Rubiera, F.; Pis, J. J. Surface modification of activated carbons for CO2 capture. *Appl. Surf. Sci.* **2008,** *254*, 7165-7172.

85. Plaza, M. G.; Pevida, C.; Arias, B.; Fermoso, J.; Casal, M. D.; Martin, C. F.; Rubiera, F.; Pis, J. J. Development of low-cost biomass-based adsorbents for postcombustion CO2 capture. *Fuel* **2009,** *88*, 2442-2447.

86. Przepiorski, J.; Skrodzewicz, M.; Morawski, A. W. High temperature ammonia treatment of activated carbon for enhancement of CO2 adsorption. *Appl. Surf. Sci.* **2004,** *225*, 235-242.

87. Shafeeyan, M. S.; Daud, W.; Houshmand, A.; Shamiri, A. A review on surface modification of activated carbon for carbon dioxide adsorption. *J. Anal. Appl. Pyrol.* **2010,** *89*, 143-151.

88. Zhang, Z. J.; Xu, M. Y.; Wang, H. H.; Li, Z. Enhancement of CO2 adsorption on high surface area activated carbon modified by N-2, H-2 and ammonia. *Chem. Eng. J.* **2010,** *160*, 571-577.

89. Verma, S. K.; Walker, P. L. Carbon molecular-sieves with stable hydrophobic surfaces. *Carbon* **1992,** *30*, 837-844.

90. Adams, L. B.; Hall, C. R.; Holmes, R. J.; Newton, R. A. An examination of how exposure to humid air can result in changes in the adsorption properties of activated carbons. *Carbon* **1988,** *26*, 451-459.

91. Menendez, J. A.; Phillips, J.; Xia, B.; Radovic, L. R. On the modification and characterization of chemical surface properties of activated carbon: In the search of carbons with stable basic properties. *Langmuir* **1996,** *12*, 4404-4410.

92. Abanades, J. C. The maximum capture efficiency of CO2 using a carbonation/calcination cycle of CaO/CaCO3. *Chem. Eng. J.* **2002,** *90*, 303-306.

93. Abanades, J. C.; Alvarez, D. Conversion limits in the reaction of CO2 with lime. *Energ. Fuel.* **2003,** *17*, 308-315.

94. Abanades, J. C.; Grasa, G.; Alonso, M.; Rodriguez, N.; Anthony, E. J.; Romeo, L. M. Cost structure of a postcombustion CO2 capture system using CaO. *Environ. Sci. Technol.* **2007,** *41*, 5523-5527.

95. Abanades, J. C.; Rubin, E. S.; Anthony, E. J. Sorbent cost and performance in CO2 capture systems. *Ind. Eng. Chem. Res.* **2004,** *43*, 3462-3466.

96. Bhagiyalakshmi, M.; Lee, J. Y.; Jang, H. T. Synthesis of mesoporous magnesium oxide: Its application to CO2 chemisorption. *Int. J. Greenh. Gas Control* **2010,** *4*, 51-56.

97. Casarin, M.; Falcomer, D.; Glisenti, A.; Vittadini, A. Experimental and theoretical study of the interaction of CO2 with alpha-Al2O3. *Inorg. Chem.* **2003,** *42*, 436-445.

98. Abee, M. W.; York, S. C.; Cox, D. F. CO2 adsorption on alpha-Cr2O3 (1012) surfaces. *J. Phys. Chem. B* **2001,** *105*, 7755-7761.

99. Hadenfeldt, S.; Benndorf, C.; Stricker, A.; Towe, M. Adsorption of CO2 on K-promoted Cu(111) surfaces. *Surf. Sci.* **1996,** *352*, 295-299.

100. Dobrova, E. P.; Bratchikova, I. G.; Mikhalenko, II Adsorption of carbon dioxide on tantalum oxide coated with palladium chloride. *Russ. J. Phys. Chem.* **2006,** *80*, 1528-1531.

101. Ismail, H. M.; Cadenhead, D. A.; Zaki, M. I. Surface reactivity of iron oxide pigmentary powders toward atmospheric components: XPS, FESEM, and gravimetry of CO and CO2 adsorption. *J. Colloid Interface Sci.* **1997,** *194*, 482-488.

102. Tutuianu, M.; Inderwildi, O. R.; Bessler, W. G.; Warnatz, J. Competitive adsorption of NO, NO2, CO2, and H2O on BaO(100): A quantum chemical study. *J. Phys. Chem. B* **2006,** *110*, 17484-17492.

103. Tai, J. R.; Ge, Q. F.; Davis, R. J.; Neurock, M. Adsorption of CO2 on model surfaces of cesium oxides determined from first principles. *J. Phys. Chem. B* **2004,** *108*, 16798-16805.

104. Doskocil, E. J.; Bordawekar, S. V.; Davis, R. J. Alkali-support interactions on rubidium base catalysts determined by XANES, EXAFS, CO2 adsorption, and IR spectroscopy. *J. Catal.* **1997,** *169*, 327-337.

105. Li, H. S.; Zhong, S. H.; Wang, J. W.; Xiao, X. F. Effect of K2O on adsorption and reaction of CO2 and CH3OH over Cu-Ni/ZrO2-SiO2 catalyst for synthesis of dimethyl carbonate. *Chin. J. Catal.* **2001,** *22*, 353-357.

106. Alcerreca-Corte, I.; Fregoso-Israel, E.; Pfeiffer, H. CO2 absorption on Na2ZrO3: A kinetic analysis of the chemisorption and diffusion processes. *J. Phys. Chem. C* **2008,** *112*, 6520-6525.

107. Mosqueda, H. A.; Vazquez, C.; Bosch, P.; Pfeiffer, H. Chemical sorption of carbon dioxide (CO2) on lithium oxide (Li2O). *Chem. Mat.* **2006,** *18*, 2307-2310.

108. Nakagawa, K.; Ohashi, T. A novel method of CO2 capture from high temperature gases. *J. Electrochem. Soc.* **1998,** *145*, 1344-1346.

109. Ida, J.; Xiong, R. T.; Lin, Y. S. Synthesis and CO2 sorption properties of pure and modified lithium zirconate. *Sep. Purif. Technol.* **2004,** *36*, 41-51.

110. Lopez-Ortiz, A.; Rivera, N. G. P.; Rojas, A. R.; Gutierrez, D. L. Novel carbon dioxide solid acceptors using sodium containing oxides. *Sep. Sci. Technol.* **2004,** *39*, 3559-3572.

111. Ochoa-Fernandez, E.; Haugen, G.; Zhao, T.; Ronning, M.; Aartun, I.; Borresen, B.; Rytter, E.; Ronnekleiv, M.; Chen, D. Process design simulation of H-2 production by sorption enhanced steam methane reforming: evaluation of potential CO2 acceptors. *Green Chem.* **2007,** *9*, 654-662.

112. Yin, X.-S.; Song, M.; Zhang, Q.-H.; Yu, J.-G. High-Temperature CO2 Capture on Li6Zr2O7: Experimental and Modeling Studies. *Ind. Eng. Chem. Res.* **2010,** *49*, 6593-6598.

113. Iwan, A.; Stephenson, H.; Ketchie, W. C.; Lapkin, A. A. High temperature sequestration of CO2 using lithium zirconates. *Chem. Eng. J.* **2009,** *146*, 249-258.

114. Ida, J.; Lin, Y. S. Mechanism of high-temperature CO2 sorption on lithium zirconate. *Environ. Sci. Technol.* **2003,** *37*, 1999-2004.

115. Pfeiffer, H.; Lima, E.; Bosch, P. Lithium-sodium metazirconate solid solutions, Li2-xNaxZrO3 (0 <= x <= 2): A hierarchical architecture. *Chem. Mat.* **2006,** *18*, 2642-2647.

116. Pfeiffer, H.; Vazquez, C.; Lara, V. H.; Bosch, P. Thermal behavior and CO2 absorption of Li2-xNaxZrO3 solid solutions. *Chem. Mat.* **2007,** *19*, 922-926.

117. Pfeiffer, H.; Bosch, P. Thermal Stability and High-Temperature Carbon Dioxide Sorption on Hexa-lithium Zirconate (Li6Zr2O7). *Chem. Mat.* **2005,** *17*, 1704-1710.

118. Nair, B. N.; Yamaguchi, T.; Kawamura, H.; Nakao, S. I.; Nakagawa, K. Processing of lithium zirconate for applications in carbon dioxide separation: Structure and properties of the powders. *J. Am. Ceram. Soc.* **2004,** *87*, 68-74.

119. Ochoa-Fernandez, E.; Ronning, M.; Grande, T.; Chen, D. Synthesis and CO2 capture properties of nanocrystalline lithium zirconate. *Chem. Mat.* **2006,** *18*, 6037-6046.

120. Ochoa-Fernandez, E.; Ronning, M.; Grande, T.; Chen, D. Nanocrystalline lithium zirconate with improved kinetics for high-temperature CO2 capture. *Chem. Mat.* **2006,** *18*, 1383-1385.

121. Ochoa-Fernandez, E.; Rusten, H. K.; Jakobsen, H. A.; Ronning, M.; Holmen, A.; Chen, D. Sorption enhanced hydrogen production by steam methane reforming using Li2ZrO3 as sorbent: Sorption kinetics and reactor simulation. *Catal. Today* **2005,** *106*, 41-46.

122. Liang, Y.; Harrison, D. P.; Gupta, R. P.; Green, D. A.; McMichael, W. J. Carbon dioxide capture using dry sodium-based sorbents. *Energ. Fuel.* **2004,** *18*, 569-575.

123. Lee, S. C.; Kim, J. C. Dry potassium-based sorbents for CO2 capture. *Catal. Surv. Asia* **2007,** *11*, 171-185.

124. Zhao, C. W.; Chen, X. P.; Zhao, C. S. Study on CO2 capture using dry potassium-based sorbents through orthogonal test method. *Int. J. Greenh. Gas Control* **2010,** *4*, 655-658.

125. Reddy, M. K. R.; Xu, Z. P.; Lu, G. Q.; da Costa, J. C. D. Layered double hydroxides for CO2 capture: Structure evolution and regeneration. *Ind. Eng. Chem. Res.* **2006,** *45*, 7504-7509.

126. Yong, Z.; Rodrigues, A. E. Hydrotalcite-like compounds as adsorbents for carbon dioxide. *Energy Conv. Manag.* **2002,** *43*, 1865-1876.

127. Reddy, M. K. R.; Xu, Z. P.; Lu, G. Q.; da Costa, J. C. D. Influence of water on high-temperature CO2 capture using layered double hydroxide derivatives. *Ind. Eng. Chem. Res.* **2008,** *47*, 2630-2635.

128. Hutson, N. D.; Speakman, S. A.; Payzant, E. A. Structural effects on the high temperature adsorption of CO2 on a synthetic hydrotalcite. *Chem. Mat.* **2004,** *16*, 4135-4143.

129. Yong, Z.; Mata, V.; Rodriguez, A. E. Adsorption of carbon dioxide onto hydrotalcite-like compounds (HTlcs) at high temperatures. *Ind. Eng. Chem. Res.* **2001,** *40,* 204-209.

130. Oliveira, E. L. G.; Grande, C. A.; Rodrigues, A. E. CO2 sorption on hydrotalcite and alkali-modified (K and Cs) hydrotalcites at high temperatures. *Sep. Purif. Technol.* **2008,** *62*, 137-147.

131. Li, H.; Eddaoudi, M.; O'Keeffe, M.; Yaghi, O. M. Design and synthesis of an exceptionally stable and highly porous metal-organic framework. *Nature* **1999,** *402*, 276-279.

132. Eddaoudi, M.; Kim, J.; Rosi, N.; Vodak, D.; Wachter, J.; O'Keeffe, M.; Yaghi, O. M. Systematic design of pore size and functionality in isoreticular MOFs and their application in methane storage. *Science* **2002,** *295*, 469-472.

133. Li, D.; Kaneko, K. Hydrogen bond-regulated microporous nature of copper complex-assembled microcrystals. *Chem. Phys. Lett.* **2001,** *335*, 50-56.

134. Bae, Y. S.; Mulfort, K. L.; Frost, H.; Ryan, P.; Punnathanam, S.; Broadbelt, L. J.; Hupp, J. T.; Snurr, R. Q. Separation of CO2 from CH4 using mixed-ligand metal-organic frameworks. *Langmuir* **2008,** *24*, 8592-8598.

135. Millward, A. R.; Yaghi, O. M. Metal-organic frameworks with exceptionally high capacity for storage of carbon dioxide at room temperature. *J. Am. Chem. Soc.* **2005,** *127*, 17998-17999.

136. Bourrelly, S.; Llewellyn, P. L.; Serre, C.; Millange, F.; Loiseau, T.; Ferey, G. Different adsorption behaviors of methane and carbon dioxide in the isotypic nanoporous metal terephthalates MIL-53 and MIL-47. *J. Am. Chem. Soc.* **2005,** *127*, 13519-13521.

137. Pan, L.; Adams, K. M.; Hernandez, H. E.; Wang, X. T.; Zheng, C.; Hattori, Y.; Kaneko, K. Porous lanthanide-organic frameworks: Synthesis, characterization, and unprecedented gas adsorption properties. *J. Am. Chem. Soc.* **2003,** *125*, 3062-3067.

CHAPTER 2

EXPERIMENTAL METHODS

2.1 Ultrasonic Spray Pyrolysis

Ultrasonic spray pyrolysis (USP) is a method for aerosol synthesis and processing of materials that can easily be scaled to the industrial level. Typically, USP uses high frequency ultrasound (~2 MHz) to generate an aerosol. The mist is carried through a furnace where evaporation and precursor decomposition occur.[1, 2] Ultrasound produces relatively uniform droplet sizes (D_d) which can be modeled by the Lang Equation (Equation 2.1):

$$D_d = 0.34 \left(\frac{8\pi\sigma}{\rho f^2}\right)^{1/3} \qquad \text{Eq. 2.1}$$

where σ is surface tension of the precursor solution (N/m), ρ is the density of the solution (kg/m^3), and f is the frequency of the ultrasound (Hz).[3, 4]

Each droplet acts as a mini-reactor and generally yields one particle per droplet.[5] Many different examples of particle structures formed by USP are available including solid spheres,[6] hollow spheres,[7] porous structures,[1] ball-in-ball spheres,[8] and nanoplateles.[9]

The formation of hollow spheres is of particular interest for this work and can be described as follows (Figure 2.1). The solvent of a nebulized droplet evaporates as the mist enters the furnace tube. Under the right conditions, solvent evaporation causes the precursor to precipitate and form a shell on the outside of the droplet. Gases evolved

from the evaporating solvent on the interior and the decomposition of the precursor template the hollow sphere and also act as porogens. As the precursor fully decomposes to the product, the sphere becomes denser. For USP done in the Suslick group, these reactions occur within the residence time inside of the furnace tube, which is usually about 10 seconds.[7]

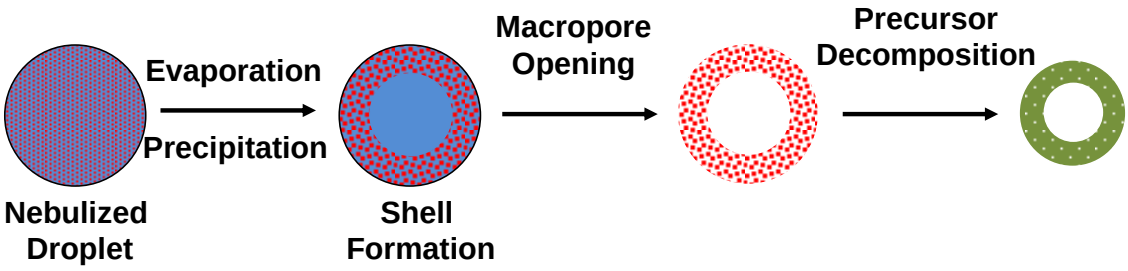

Figure 2.1 Mechanism for the formation of hollow particles via USP.

2.2 Apparatus

The USP setup is represented in Figure 2.2. The custom nebulizer base was constructed at the University of Illinois at Urbana-Champaign electronics shop. It is equipped with a replaceable nebulizer board (APC International, Inc., # 50-1011) with a piezoceramic which operates at a fixed frequency of 1.65 MHz. A silicone O-ring provides a waterproof seal between the nebulizer board and the casing. Water is added above the piezoceramic so that the ultrasound has a medium to travel through. The water level must be at least 30 mm to protect the piezoceramic. Consequently, the base is outfitted with a floating switch that turns the unit off should the water level decrease below 30 mm. The casing is fitted with four pegs to keep the USP atomization cell centered above the piezoceramic. Finally, the intensity of the ultrasound can be controlled by a variac knob positioned on the front of the casing. Although the nebulizer

base was custom-built, a common household humidifier base was previously used and shown to be equally effective.[5]

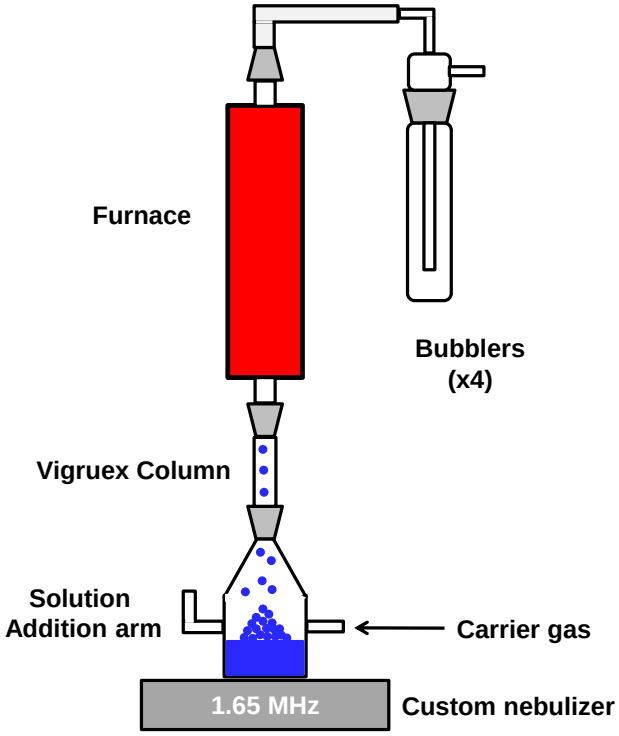

Figure 2.2 Scheme of the USP apparatus.

The atomization cell was fabricated by the University of Illinois at Urbana-Champaign glass shop. It is constructed from a 57 mm O-ring flat flange (Chemglass, # CG-138-02) which tapers to a 24/40 ground glass joint at the top. Additionally, the cell is outfitted with a gas inlet arm and a solution addition arm. The threads of the gas inlet arm are wrapped with Teflon tape before the gas hose is attached to create a better seal. The addition arm is wired shut using copper wire and a #9 Subaseal. A circular plastic membrane cut from a zip-lock bag (2 mils) is clamped to the base of the atomization cell using a custom clamp (Figure 2.3). The clamp consists of a base brass ring with 6 equally spaced holes (1/4 in. diameter) for socket-hedge cap screws (1/4 in. o.d., 2 in. length) on to which a Teflon ring with an O-ring groove is placed. A Viton O-ring (CG-

305-331) is placed in the groove under the membrane. Finally, the atomization cell is set on top of the membrane and is clamped with two half-moon Teflon pieces and two half-moon brass pieces, each with three holes that align with the screws from the base. The clamp is secured with six washers and nuts.

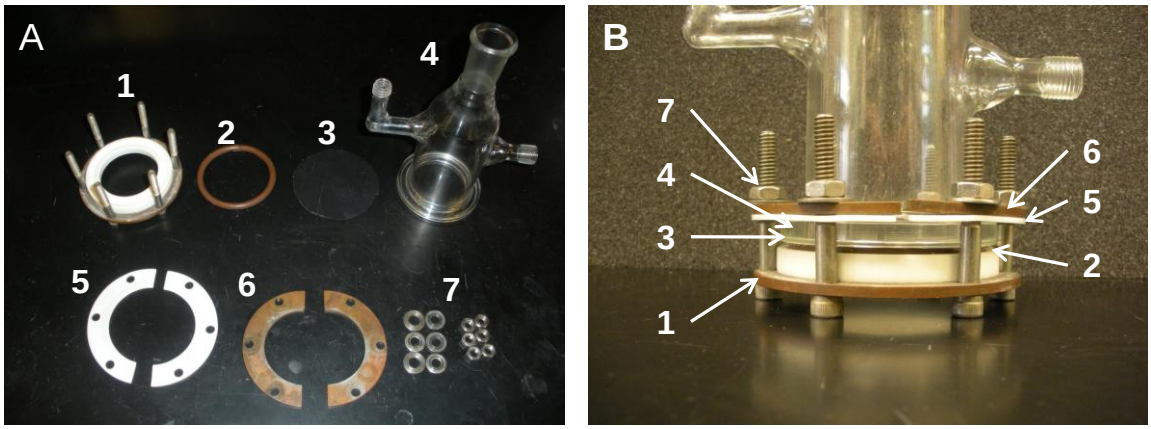

Figure 2.3 (A) Parts of the custom clamp and **(B)** the custom clamp assembled for USP. 1 = base brass ring, 2 = O-ring, 3 = polyethylene membrane (2 mils), 4 = nebulization cell, 5 = Teflon pieces, 6 = brass pieces, 7 = washers and nuts.

A 2 in. Vigreux column is inserted into the 24/40 joint of the atomization cell. The Vigreux column helps keep the droplet size uniform by condensing the larger droplets on the internal fingers of the column. Inserted into the top 24/40 joint of the Vigreux column is a custom quartz furnace tube (length = 450 mm, I.D. = 32 mm, O.D. = 35 mm) which runs through a furnace (Omega CRFC-212/120-C-A High Temperature Cylindrical Heater) and ends in a 35/25 ball joint. The furnace is controlled by a Honeywell UCD 3000 controller and the temperature in monitored by inserting a K-type thermocouple into the top of the furnace. The thermocouple is wedged between the quartz furnace tube and the furnace at the hottest place in the furnace, approximately 1/3 of the distance from the top.

A socket joint which tapers to a tube fitting is clamped to the top of the furnace tube. A series of four bubblers are connected using Tygon tubing for product collection. The final bubbler is vented out through the fume hood.

2.3 Solution Preparation

All solutions were prepared volumetrically. Because the solvent was ethanol, the solution was added by syringe through the atomization cell addition arm in 25 mL aliquots once the furnace equilibrated at the appropriate temperature. This minimized increasing the concentration of the precursor due to ethanol evaporation (ultrasonic distillation).

2.4 Product Collection and Isolation

The product was collected in collection bubblers containing ~50 mL of 95% ethanol. At the end of the reaction, the contents of the bubblers were transferred into at 500 mL round bottom flask (RBF) and concentrated to ~25 mL on a Buchi Rotavapor R-124 rotary evaporator at 150 mbar and ~50 °C. The product was transferred with ethanol out of the RBF and into a 50 mL centrifuge tube and concentrated on a Fisher Scientific Centrific Centrifuge at maximum speed for 12 min. The supernatant was decanted and the product was transferred with ethanol into a 20 mL scintillation vial and dried on the rotary evaporator at 180 mbar and ~50 °C. Finally, the powder was scratched from the sides of the vial and dried in a vacuum oven at ~80 °C for a minimum of 4 hours.

2.5 Materials Characterization

2.5.1 Scanning Electron Microscopy

Scanning electron micrographs (SEM) were taken using a Hitachi S4800 SEM at an accelerating voltage of 10 kV and a working distance of 8 mm. Samples were prepared by suspending a small amount of powder in ethanol using a sonication bath (50/60 Hz Branson Ultrasonic Cleaning Bath). Four drops of the suspension were drop cast on each side of a small piece of aluminum foil via pipette. The sample was left to dry overnight in air. Prior to imaging, the sample was coated with a Au-Pd alloy using an Emitech K575 metal evaporator to reduce the effects of sample charging.

2.5.2 Transmission Electron Microscopy

Transmission electron micrographs (TEM) were taken using a JEOL 2100 Cryo TEM at an operating voltage of 200 kV. Samples were prepared by suspending a small amount of powder in ethanol using a sonication bath (50/60 Hz Branson Ultrasonic Cleaning Bath). Four drops of the suspension were drop cast onto a lacey carbon copper TEM grid (Ted Pella, Inc. #01881-F). The samples were then allowed to dry overnight in air.

2.5.3 Powder X-ray Diffraction

Powder X-ray diffractograms were obtained by using a Siemens-Bruker D5000 XRD. The instrument uses Cu Kα radiation ($\lambda = 1.5418$ Å) and operates at 40 kV and 30 mA. Typically, diffraction patterns were captured using a scan speed of 1 deg/min at a

step size of 0.02 deg between 2θ = 10 and 90. Analysis of the patterns was completed using Jade X-ray analysis software.

Samples were prepared by first grinding the sample into a fine powder. This made the sample easier to pack into the low-background sample holder well.

2.5.4 Surface Area Analysis

Surface area measurements were obtained using a 3-point BET (Brunauer, Emmett, Teller) N_2 adsorption curve on a Quantachrome Instruments Nova 2200e Surface Area and Pore Analyzer. Ultra high purity (UHP) N_2 was the adsorption gas and was condensed at -196 ºC. Samples were degassed at 120 °C for at least 12 hours in the instrument's degassing stations prior to surface analysis.

2.5.5 Thermogravametric Analysis

Thermogravamentric analysis (TGA) was conducted on a Thermo Scientific VersaTherm thermogravametric analyzer. The instrument is equipped with two ports for reaction gases. The flow rate of the gases is controlled by rotometers. Approximately 20 mg of sample was loaded into a quartz sample boat. The instrument is controlled using Thermal Analyst Data Acquisition Version 3.30.0 VT software which allows the user to program the TGA operation parameters. A typical method is as follows (Figure 2.4): (1) heat from room temperature to 250 °C at 40 deg/min under N_2 (2) hold at 250 °C for 20 min under N_2 (this is to remove any water vapor or other adsorbents) (3) heat from 250 °C to 900 °C at 40 deg/min under N_2 (4) hold at 900 °C for 5 min under N_2 (this is the calcination stage) (5) cool from 900 °C to 650 °C at -20 deg/min under N_2 (6) hold at

650 °C for 5 min under N_2 (7) maintain the temperature at 650 °C and switch the gas to CO_2 for 30 min (this is the carbonation stage) (8) maintain the temperature at 650 °C and switch the gas back to N_2 for 5 min (9) heat from 650 °C to 900 °C at 20 deg/min under N_2 (10) repeat steps 4-9. The sample was saved after TGA cycling for post-cycling characterization. TGA data was analyzed using Thermo Cahn Instruments Thermal Analyst Version 1.3.2.2 software.

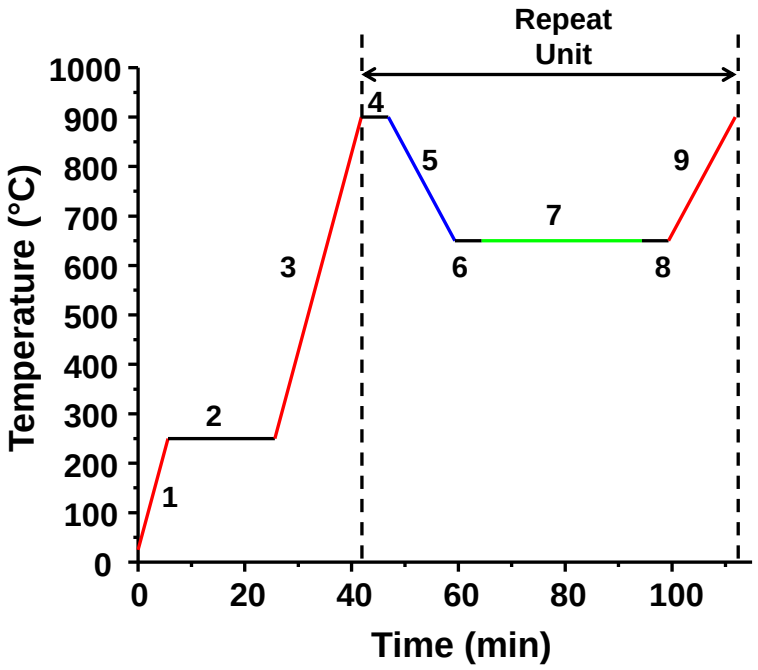

Figure 2.4 Diagram of the method programed for multiple carbonation/calcination cycles. Red corresponds to heating, black to isothermal periods under N_2, blue to cooling, and green to isothermal periods under CO_2.

2.6 References

1. Skrabalak, S. E.; Suslick, K. S. Porous Carbon Powders Prepared by Ultrasonic Spray Pyrolysis. *J. Am. Chem. Soc.* **2006,** *128,* 12642-12643.

2. Bang, J. H.; Suslick, K. S. Applications of Ultrasound to the Synthesis of Nanostructured Materials. *Adv. Mater.* **2010,** *22,* 1039-1059.

3. Kodas, T. T.; Hampden-Smith, M., *Aerosol Processing of Materials*. Wiley-VCH: New York, 1999.

4. Lang, R. J. Ultrasonic atomization of liquids. *J. Acoust. Soc. Am.* **1962,** *34*, 6-8.

5. Skrabalak, S. Porous Materials Prepared by Ultrasonic Spray Pyrolysis. University of Illinois at Urbana-Champaign, Urbana, 2007.

6. Xia, B.; Lenggoro, I. W.; Okuyama, K. Novel Route to Nanoparticle Synthesis by Salt-Assisted Aerosol Decomposition. *Adv. Mater.* **2001,** *13*, 1579-1582.

7. Fortunato, M. E.; Rostam-Abadi, M.; Suslick, K. S. Nanostructured Carbons Prepared by Ultrasonic Spray Pyrolysis. *Chem. Mat.* **2010,** *22*, 1610-1612.

8. Suh, W. H.; Jang, A. R.; Suh, Y. H.; Suslick, K. S. Porous, hollow, and ball-in-ball metal oxide microspheres: Preparation, endocytosis, and cytotoxicity. *Adv. Mater.* **2006,** *18*, 1832-1837.

9. Mann, A. K. P.; Skrabalak, S. E. Synthesis of Single-Crystalline Nanoplates by Spray Pyrolysis: A Metathesis Route to Bi2WO6. *Chem. Mat.* **2011,** *23*, 1017-1022.

CHAPTER 3

HOLLOW, POROUS CALCIUM OXIDE PREPARED BY ULTRASONIC SPRAY PYROLYSIS

3.1 Introduction

This chapter presents an overview of recent advances in carbon dioxide capture using calcium oxide sorbents. CaO materials were synthesized by USP and the performance of these materials as CO_2 sorbents was evaluated based upon their stability over multiple calcination/carbonation cycles and compared to commercially available calcium carbonates. The effects of adding aluminum- or magnesium-based binders on the cyclic stability and capacity of the sorbents were also investigated.

3.1.1 Calcium Oxide

Calcium oxide materials have been of significant interest as sorbents for high temperature CO_2 capture from flue gas in recent years because CaO has a very high capacity for CO_2 (17.8 mmol g^{-1}) and calcium minerals are extremely abundant in the form of limestone.[1] Calcium oxide reacts with carbon dioxide to form calcium carbonate in a reversible manner (Equation 3.1).[2]

$$CaO_{(s)} + CO_{2(g)} \rightleftharpoons CaCO_{3(s)} \quad \Delta H_{r,\,298\ K} = -178\ kJ/mol \qquad \text{Eq. (3.1)}$$

In 1973 Barker reported that the carbonation process does not fully reach equilibrium. He found that the amount of CO_2 captured dropped significantly as CaO

was cycled up to 40 times and he attributed this decreased capacity to loss of pore volume and sintering. Barker also reported that carbonation initially occurred very rapidly, however, the reactivity of the sorbent subsequently decreased over time (Figure 3.1) due to the formation of a carbonate shell through which the rate of reaction was controlled by diffusive processes. The carbonate shell was observed to be 22 nm in thickness, which led Barker to hypothesize that a CaO particle less than 44 nm in diameter would show improved reactivity.[3] Later, Barker supported his hypothesis by reporting that 10 nm CaO particles showed no decrease in capacity over 30 cycles.[4]

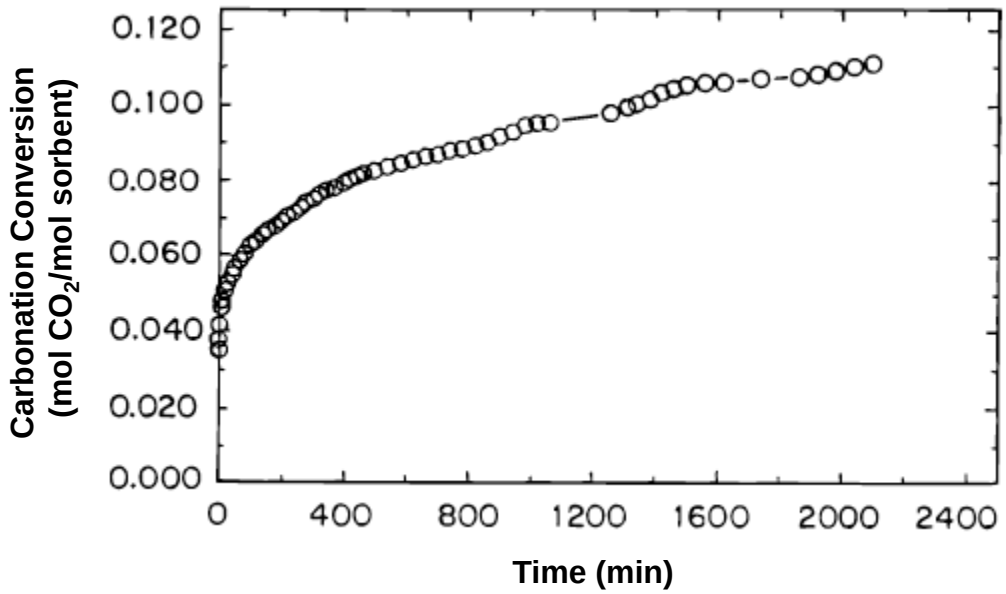

Figure 3.1 Typical CO_2 capture curve for CaO. Carbonated at 600 °C in 100% CO_2.[5]

Since Barker's report, many studies have been conducted on pure CaO to test its stability as a sorbent. Gupta and Fan synthesized precipitated calcium carbonate (PCC) by bubbling CO_2 through a slurry of $Ca(OH)_2$.[6] They found that the mesoporous sorbent retained 90% of its theoretical CO_2 capacity after two cycles at 700 °C, whereas commercial $CaCO_3$ dropped to 64% after two cycles under the same conditions. Lu

screened a series of precursors and found that CaO materials calcined from calcium acetate had the highest surface areas and best conversion after 27 cycles.[7] Yang and coworkers synthesized hollow nanopods that retained 60% of their capacity after 50 cycles.[8] In studies where extended cycles were conducted (between 200 and 500 cycles) it was found that a residual capacity for CO_2 of around 8% remained, regardless of the cycling conditions.[9, 10] Abanades pointed out, however, that many laboratory tests of pure CaO materials are done under mild conditions. Under realistic conditions where temperatures exceed 900 °C and the atmosphere is 100% CO_2 for calcination, most CaO materials perform very pooly.[11]

3.1.2 Modeling Sorbent Degradation

Several models for CaO sorbent degradation have been developed. Abanades and Alvarez compiled the data from several researchers, each of whom saw a dramatic decrease in CO_2 capacity after the first cycle (Figure 3.2). They developed a model based on the loss of microporosity and gain of meso- and macroporosity which fit the experimental data very well.[12, 13] Other models have been developed which attribute capacity loss in the sorbents largely to sintering of the $CaCO_3$ particles.[14-16] This is expected because the Tammann temperature—the temperature at which sintering becomes significant—is 533 °C for $CaCO_3$.[17] Generally, calcination occurs at temperatures exceeding 700 °C.[1] Researchers agree that that the general loss of sorbent surface area reduces the CO_2 capture capacity, regardless of whether the model describes capacity loss primarily to micropore filling or to particle sintering.

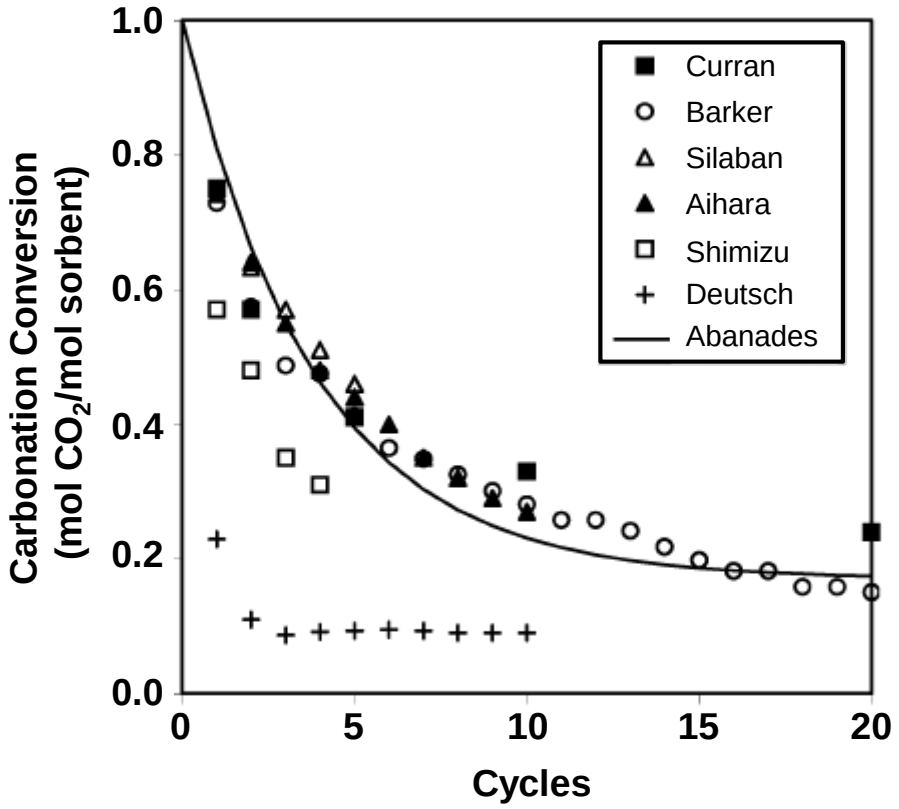

Figure 3.2 Several studies on the degradation of CaO sorbent capacity for CO_2 over multiple cycles from the work of Curran,[18] Barker,[3] Silaban,[19] Aihara,[20] Shimizu,[21] Deutsch,[22] and the equation proposed by Abanades.[13] Data compiled by Abanades.[13]

Models have also been developed to describe the carbonation curve shown in Figure 3.1. The initial rate is a rapid, chemically controlled process.[1] Bhatia and Perlmutter attributed the slower rate at temperatures below 500 °C to the diffusion of CO_3^{2-} ions through the carbonate layer. To maintain electroneutrality, the O^{2-} ion is proposed to diffuse outward (Equations 3.2 and 3.3). At temperatures above 500 °C, CO_3^{2-} is proposed to decompose to CO_2 and O^{2-}. The CO_2 produced is expected to carbonate neighboring CaO sites toward the interior of the particle.[23] Another mechanism proposes that CO_2 diffuses along grain boundaries and imperfections in the crystal structure.[5]

$$CO_3^{2-} + CaO \rightarrow CaCO_3 + O^{2-} \quad \text{Eq. (3.2)}$$

$$(CO_2)_{ads} + O^{2-} \rightarrow CO_3^{2-} \quad \text{Eq. (3.3)}$$

3.1.3 Binders and Supports for Calcium Oxide

A significant effort has been directed toward improving the stability of CaO sorbents over a large number of cycles. Much work has focused on loading CaO onto various supports[20, 24-26] or incorporating binders into the sorbent.[27-38]

Wu and coworkers loaded 18.5 wt% CaO onto a porous carbon support. [26] This was the first sorbent synthesized that captured CO_2 via both physi- and chemisorption methods. After cycling between 600 and 750 °C 10 times, the sorbent retained 70% of its capacity. The improved capacity was attributed to the porous carbon support isolating the nanocrystals in the pores and preventing them from agglomerating.

Recently, there has been a great interest in incorporating aluminum as a binder for CaO sorbents.[28, 29, 33-35, 37, 39] Li and coworkers found that sorbents which contain a mayenite binder ($Ca_{12}Al_{14}O_{33}$) retained 75% of maximum capacity after 13 cycles.[29] Further investigation showed that the sorbent retained 22% of its capacity when cycled 50 times under more realistic conditions (980 °C, 100% CO_2 for calcination).[28] Other inert binder materials incorporated into CaO sorbents include MgO,[30] Cs_2O,[36] ZrO_2,[31] and La_2O_3.[32]

3.1.4 Effects of Hydration

Instead of decreasing the CaO content in sorbents by adding binders or supports, it has been found that sorbents can be regenerated by periodic hydration treatments. The

incorporation of a hydration step between the calcination and carbonation steps has been reported to form a eutectic of calcium salts at high pressures (6 MPa). This allows for more complete and faster carbonation.[40] Hydrating CaO also causes the molar volume to expand by a factor of roughly two.[2] Multiple studies have shown that this causes particle fracture and effectively increases the available surface area for reaction with CO_2.[41-43] While this improves CaO capacity over multiple cycles, there are difficulties associated with the commercialization of this technique because the pulverization of the sorbent material can lead to rapid mass loss in a fluidized bed reactor.[39, 42]

3.2 Experimental

3.2.1 Materials and Equipment

The USP products were synthesized according to the techniques outlined in Chapter 2. Aluminum nitrate nonahydrate (purity ≥ 98%) and calcium nitrate tetrahydrate (purity 99%) were purchased from Aldrich and used without further purification. Magnesium nitrate hexahydrate (certified ACS grade) was purchased from Fisher and used without further purification. Argon gas from S.J. Smith was used as received.

3.2.2 Preparation of Hollow Calcium Carbonate by USP

Approximately 50 mL of a 0.25 M $Ca(NO_3)_2 \cdot 4H_2O$ solution in 95% ethanol was nebulized in the USP setup described in Chapter 2 at 600 °C. The solid, white product was collected in bubblers containing 95% ethanol and isolated according to the procedure

detailed in Chapter 2. The hollow USP $CaCO_3$ product was then dried under vacuum for ~12 h at ~80 °C prior to characterization.

3.2.3 Preparation of Al-doped Calcium Carbonate by USP

$Ca(NO_3)_2 \bullet 4H_2O$ and $Al(NO_3)_3 \bullet 9H_2O$ were dissolved in 95% ethanol such that the combined concentration of Ca^{2+} and Al^{3+} ions was 0.25 M. The aluminum content was varied such that the resulting mayenite phase ranged from 0 to 100 weight percent. This precursor solution was nebulized in the USP setup described in Chapter 2 at 600 °C. The solid, white product was collected in bubblers containing 95% ethanol and isolated according to the procedure detailed in Chapter 2. The product was then dried under vacuum for ~12 h at ~80 °C prior to characterization.

3.2.4 Preparation of Mg-doped Calcium Carbonate by USP

$Ca(NO_3)_2 \bullet 4H_2O$ and $Mg(NO_3)_2 \bullet 6H_2O$ were dissolved in 95% ethanol such that the combined concentration of Ca^{2+} and Mg^{2+} ions was 0.25 M. This precursor solution was nebulized into a white mist in the USP setup described in Chapter 2 at 600 °C. The solid, white product was collected in bubblers containing 95% ethanol and isolated according to the procedure detailed in Chapter 2. The product was then dried in the vacuum oven for ~12 h at ~80 °C prior to characterization.

3.3 Results and Discussion

3.3.1 Experimental Design

3.3.1.1 Hollow Morphology

The carbonation of CaO to $CaCO_3$ results in a 2.2-fold increase in volume.[2] This expansion causes two problems for CaO materials used for CO_2 adsorption: 1) pore blockage due to expansion of the carbonate layer over the CaO[12] and 2) loss of sorbent in a fluidized bed reactor due to particle fragmentation.[39]

A hollow morphology, which is easily obtained by USP, could overcome these problems because a hollow center could allow for particle expansion both inward and outward during CaO carbonation (Figure 3.3). This may retard pore closer to allow for faster and more complete carbonation. Additionally, the hollow structure could help reduce the amount of sorbent that is entrained in the gas stream as fine particulates due to particle fracture upon expansion.

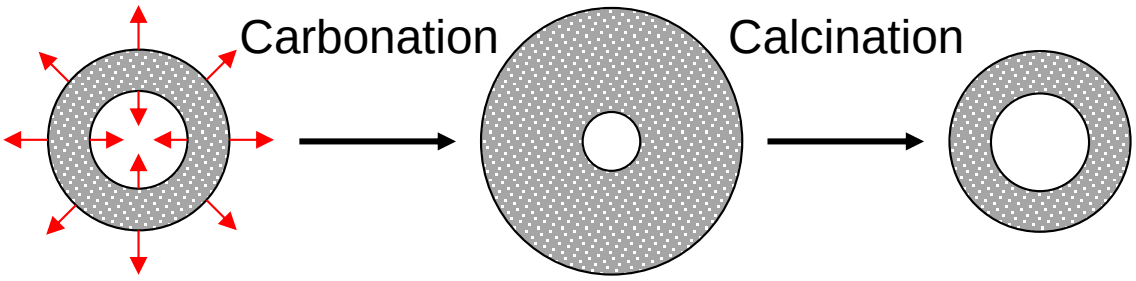

Figure 3.3 Diagram of particle expansion both inward and outward for hollow particles.

3.3.1.2 Precursor Selection

Calcium nitrate tetrahydrate [$Ca(NO_3)_2 \cdot 4H_2O$] was selected as the precursor for the preparation of porous spheres by USP. Hollow spheres were obtained according to the mechanism detailed in Chapter 2. The gas evolved from the decomposition of $Ca(NO_3)_2 \cdot 4H_2O$ acts as a porogen during particle formation, which leads to high surface area sorbents.[44] Additionally, the nitrate salt is very soluble in many common, environmentally friendly solvents, such as ethanol and water.

3.3.1.3 Solvent Selection

Water was initially used as the precursor solvent in the USP synthesis of CaO. SEM showed that the products collected from the bubblers were non-spherical agglomerates, which are atypical of USP synthesis (Figure 3.4 A). Particles isolated from the sides of the furnace tube, however, were spherical (Figure 3.4 B). These results suggested that, although calcium salts are generally insoluble in water, the water from the precursor solution collects in the bubblers and leads to a very rapid ripening process that destroys the structure of the USP products. Product collection under basic conditions did not slow the ripening process.

The system was modified to use ethanol as the precursor solvent and as the collection fluid in the bubblers, which eliminated ripening due to water. However, XRD revealed that the product isolated from the ethanol was $CaCO_3$ (Figure 3.5), and elemental analysis confirmed that the material was 100% carbonated (carbon and calcium content agreed with theoretical values for $CaCO_3$). CaO was the expected product because $Ca(NO_3)_2 \cdot 4H_2O$ decomposes to CaO at temperatures greater than 550 °C and

argon was used as the carrier gas. $CaCO_3$ was obtained because enough CO_2 was produced from the pyrolysis of ethanol to carbonate the product, with a minor contribution of CO_2 from the combustion of ethanol with the small amount of O_2 produced as the nitrate decomposes. Consequently, all reported USP products produced from an ethanol precursor solution are calcium carbonate.

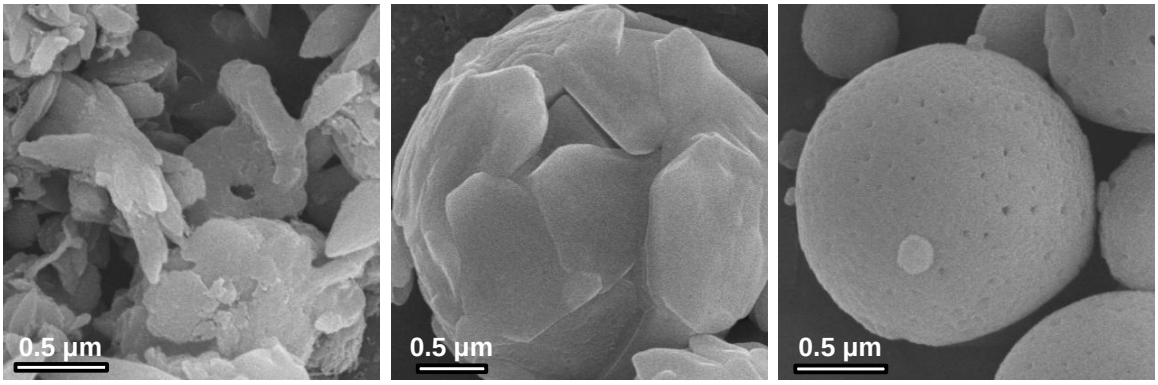

Figure 3.4 SEM images of calcium products made by USP. **(A)** Synthesized from an aqueous solution and collected in the bubblers. **(B)** Synthesized from an aqueous solution and collected from the furnace tube. **(C)** Synthesized from an ethanol solution and collected in the bubblers.

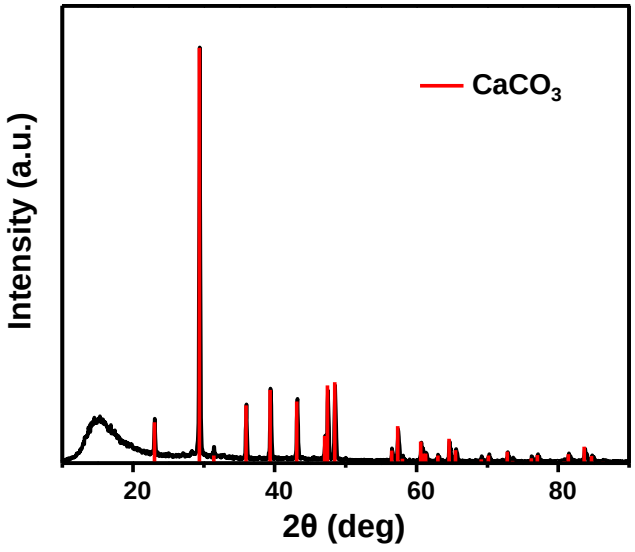

Figure 3.5 XRD of $CaCO_3$ isolated from the USP bubblers.

3.3.1.4 Cycling Conditions on the TGA

The calcination and carbonation conditions on the TGA can greatly affect the performance of the sorbent over multiple cycles. Calcium carbonate synthesized by USP under the conditions listed in Table 3.1 (hereafter referred to as USP $CaCO_3$) was subjected to four different carbonation-calcination methods and (15 cycles each). The methods are listed in Table 3.2 and the sorbent stability results are shown in Figure 3.6.

Parameter	Setting
Precursor	$Ca(NO_3)_2 \cdot H_2O$
Solvent	Ethanol
Concentration	0.25 M
Temperature	600 °C
Bubblers	Ethanol
Carrier Gas	Argon
Flow Rate	1 SLPM*

Table 3.1 Conditions under which USP $CaCO_3$ was synthesized for TGA cycling. *Standard Liter Per Minute.

Generally, the sorbent was more stable when the calcination time was short (e.g. 5 min.). Additionally, decreasing the calcination temperature from 900 °C to 800 °C increased the capacity of the sorbent over multiple cycles. Method 4, however, clearly resulted in the best sorbent stability which is likely due to a combination of the lower carbonation temperature (650 °C) and the 5 min. nitrogen purge segments before and after the carbonation period. These purge segments allow the TGA to equilibrate at the set temperature and clear any lingering reactive gases from the reaction chamber.

Method 4 was used to complete all cycling tests on the sorbents synthesized by USP. It should be noted, however, that these conditions are ideal laboratory conditions and not realistic CO_2 capture conditions. Under realistic conditions, the flue gas stream

would contain less than 30% CO_2 for carbonation and calcination would occur in a 100% CO_2 atmosphere at temperature higher than 900 °C.[11]

Step	Method 1	Method 2	Method 3	Method 4
Heat to Calcine	20 °C/min CO_2	20 °C/min N_2	20 °C/min N_2	20 °C/min N_2
Equilibrate	2 min CO_2	N/A	N/A	N/A
Calcine	900 °C 10 min N_2	900 °C 5 min N_2	800 °C 10 min N_2	900 °C 5 min N_2
Cool to Carbonate	-20 °C/min N_2	-20 °C/min N_2	-20 °C/min N_2	-20 °C/min N_2
Equilibrate	2 min N_2	2 min N_2	N/A	5 min N_2
Carbonate	700 °C 20 min CO_2	700 °C 30 min CO_2	700 °C 35 min CO_2	650 °C 30 min CO_2
Equilibrate	N/A	N/A	N/A	5 min N_2

Table 3.2 A list of the conditions under which the sorbent was cycled for each method.

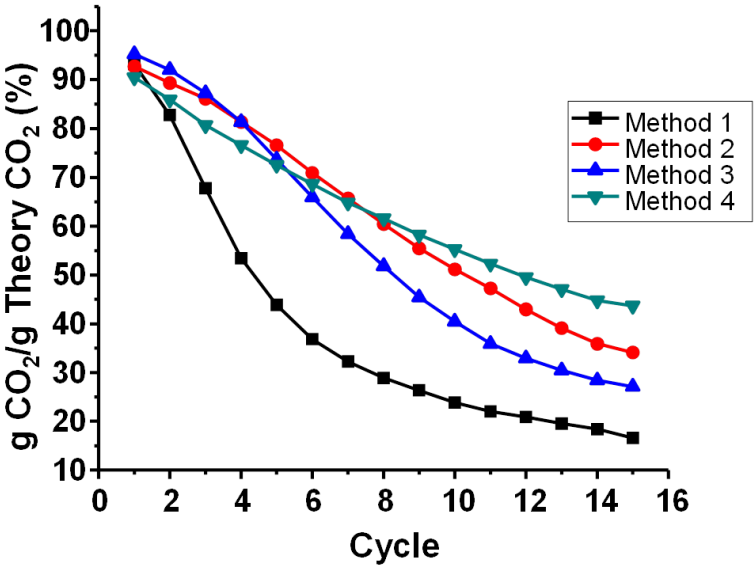

Figure 3.6 Effect of the cycling conditions on USP $CaCO_3$ cyclic stability after 15 cycles.

3.3.2 Control Over Calcium Carbonate Structure

Particle structure has been shown to have an effect on the stability of CaO materials for CO_2 capture over multiple cycles.[8] Although methods have recently been developed to control the structure of $CaCO_3$, these structures were not calcined to CaO for CO_2 capture and they were prepared by cumbersome templating methods.[45-47] USP offers control over the $CaCO_3$ structure in a facile manner and without the use of sacrificial templates. Here, the effects of furnace temperature, precursor solution concentration, and precursor solvent composition on particle structure are reported.

3.3.2.1 Effect of Furnace Temperature

No product was obtained from USP at 400 °C or 500 °C, which was expected because these temperatures are below the decomposition temperature of $Ca(NO_3)_2$ (550 °C).[44] A white, solid product was obtained from USP at 600 °C and TEM images revealed that this solid was composed of hollow $CaCO_3$ spheres (Figure 3.7 A). Similar structures were obtained from USP at 700 °C. At 800 °C, however, there was a clear change in particle morphology (Figure 3.7 B). Instead of hollow particles, slightly elongated, macroporous particles were produced (Figure 3.7 C). This structure change was likely induced by the increased rate of evaporation of the solvent and precipitation/decomposition of the precursor.

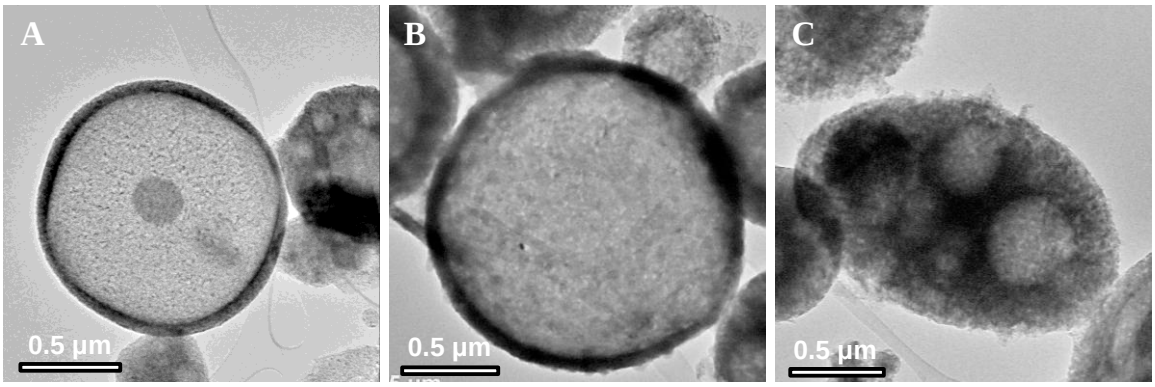

Figure 3.7 TEM images of USP $CaCO_3$ synthesized at different furnace temperatures: **(A)** 600 °C, **(B)** 700°C, and **(C)** 800 °C.

3.3.2.2 Effect of Precursor Solution Concentration

The range of precursor concentrations that can be investigated by USP is limited by the ability of the ultrasound to nebulize the solution. Three different concentrations of $Ca(NO_3)_2 \cdot 4H_2O$ in 95% ethanol nebulized using 1.65 MHz ultrasound were studied: 0.125 M, 0.25 M, and 0.50 M. A concentration of 0.75 M was also investigated, however this solution was too viscous to nebulize. At concentrations between 0.25 M and 0.50 M, the solution nebulizes very poorly.

TEM images of the resulting particles from each of the three precursor solutions reveal the interior particle structure (Figure 3.8). The particles formed from a 0.125 M solution and a 0.25 M solution have similar morphologies: both precursor solutions produced a mixture of hollow and large macropore-containing, spherical particles ~1 µm in diameter. The particles produced from a 0.50 M precursor solution were a mixture for ~50% hollow spheres and ~50% football-shaped with a hollow center. The mechanism of formation of these football-shaped particles has not yet been determined.

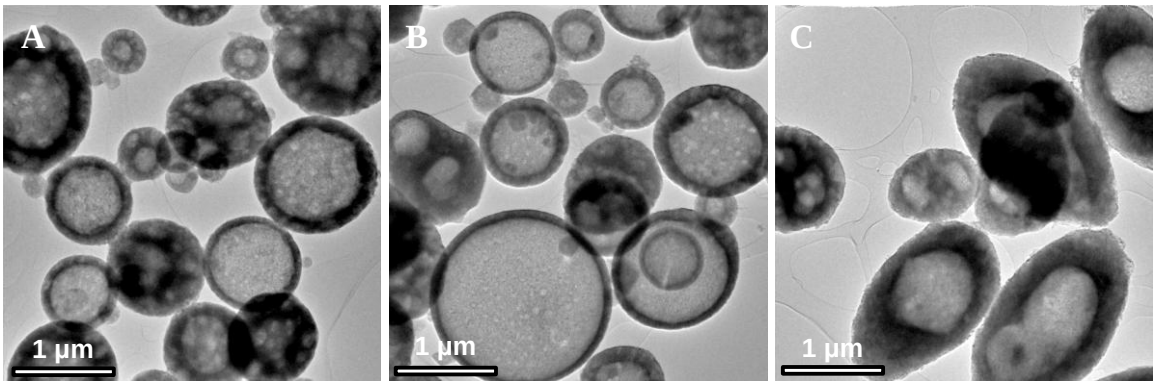

Figure 3.8 TEM images of USP $CaCO_3$ synthesized from **(A)** 0.125 M, **(B)** 0.25 M, and **(C)** 0.50 M solutions of $Ca(NO_3)_2 \cdot 4H_2O$ in 95% ethanol.

3.3.2.3 Effect of Precursor Solvent Composition

Experiments were conducted to determine the effect of various concentrations of water in the precursor solution on the structure of the USP $CaCO_3$. Particles were produced from solutions of $Ca(NO_3)_2 \cdot 4H_2O$ in 0%, 6.7%, 10%, and 20% water content (by volume) in ethanol (Figure 3.9). With the exception of the 6.7% water content solution, solutions were prepared by first dehydrating $Ca(NO_3)_2 \cdot 4H_2O$ at 230 °C for 30 min. under argon. $Ca(NO_3)_2$ was then dissolved volumetrically in the appropriate amount of water and 200 proof ethanol. The 6.7% water content solution was prepared by dissolving $Ca(NO_3)_2 \cdot 4H_2O$ in 95% ethanol (the additional 1.7% water content originates from the waters of hydration).

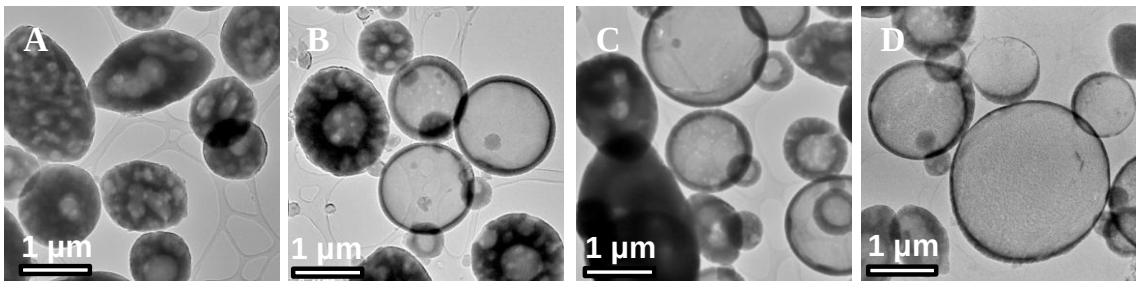

Figure 3.9 TEM images showing the effect on USP $CaCO_3$ particle structure of varying amounts of water in the ethanol precursor solution. **(A)** 0% H_2O. **(B)** 6.7% H_2O. **(C)** 10% H_2O. **(D)** 20% H_2O.

TEM images showed that macroporous particles were produced from the 0% water precursor solution; no particles with a discrete hollow center were visible. The 6.7% water content precursor solution produced a mixture of roughly 1:1 macroporous and hollow particles; the 10% water content precursor solution produced a similar ratio of particles. At 20% water content the majority of the particles were hollow with some macroporous particles present. The diameters of the hollow particles were larger than those produced from the 10% water content solution.

A mechanism related to solvent vapor pressure is proposed for the water content series as an isolated set of experiments. Ethanol, with a lower boiling point, evaporates from the droplet first. The decrease in solvent volume causes the $Ca(NO_3)_2$ to precipitate at the edge of the droplet. The water is concentrated in the center of the droplet, and subsequent water evaporation causes the particle to expand and form a hollow shell. In the case of the 0% water content precursor or in droplets where the water content is extremely low, the water is non-existent or dispersed throughout the droplet instead of concentrated in the center, so large macropores are formed instead of a hollow center. This may explain the different particle structures that appear in the products from 6.7% and 10% H_2O precursor solutions.

The proposed mechanism suggests that a high vapor pressure precursor solvent should yield hollow spheres while a low vapor pressure solvent should produce macroporous spheres. However, when the solvent was changed from water to 10% vol. butanol (boiling point 118 °C) in ethanol, macroporous spheres were obtained. A solution of 10% ethylene glycol (boiling point 197 °C) in ethanol yielded hollow spheres, but the large number of platelets or shards from broken spheres show that these spheres

are thin or especially fragile. A solution of $Ca(NO_3)_2$ in 100% methanol (boiling point 65 °C) produced hollow spheres and shards similar to those obtained from the 10% ethylene glycol solution, while a solution of 100% 1-propanol (boiling point 97 °C) yielded macroporous spheres similar to those obtained from the 10% butanol solution. These results suggest that the full mechanism for particle formation is a complex relationship between solvent vapor pressure and precursor solubility.

3.3.2.4 Effect of Structure on Sorbent Stability

The series of $CaCO_3$ sorbents synthesized from precursor solutions containing various amounts of water in ethanol described in Section 3.3.2.3 were tested using Method 4 (Section 3.3.1.4) to determine if the differences in the particle morphologies have an effect on the sorbent stability. There is no strong correlation between the particle structure (macroporous vs. hollow) and the stability of the sorbent over 15 cycles (Figure 3.10). SEM images of the sorbent from the 6.7% H_2O precursor solution, which are representative of the four sorbents tested, before and after 15 cycles clearly show severe sintering and loss of original morphology (Figure 3.11).

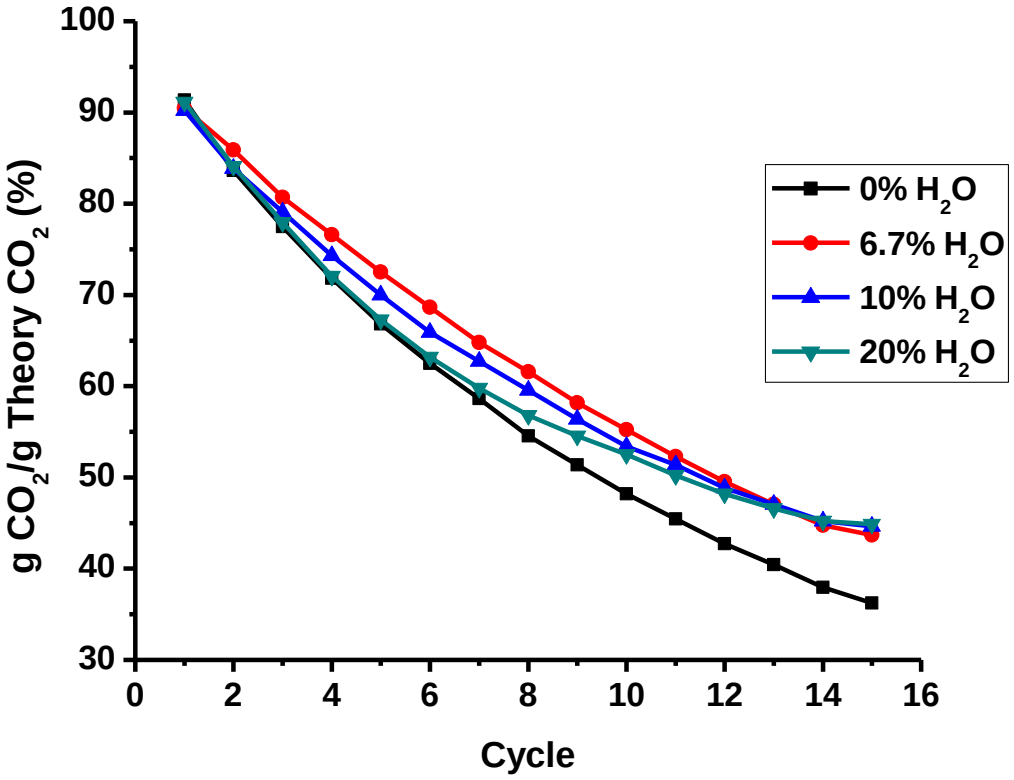

Figure 3.10 The sorbent stability of USP $CaCO_3$ synthesized from different precursor solutions.

The stability of USP $CaCO_3$ was compared to that of $CaCO_3$ obtained from Fisher Scientific and 3 μm $CaCO_3$ produced by CalCarb. After 15 cycles, the USP $CaCO_3$ retained the highest capacity of the three. The 3 μm sorbent is approximately the same size as the USP sorbent (~1 μm), so the improved stability is not exclusively due to the reduced size of the USP particles. The hollow, porous structure of the USP sorbent offers additional stability over multiple cycles.

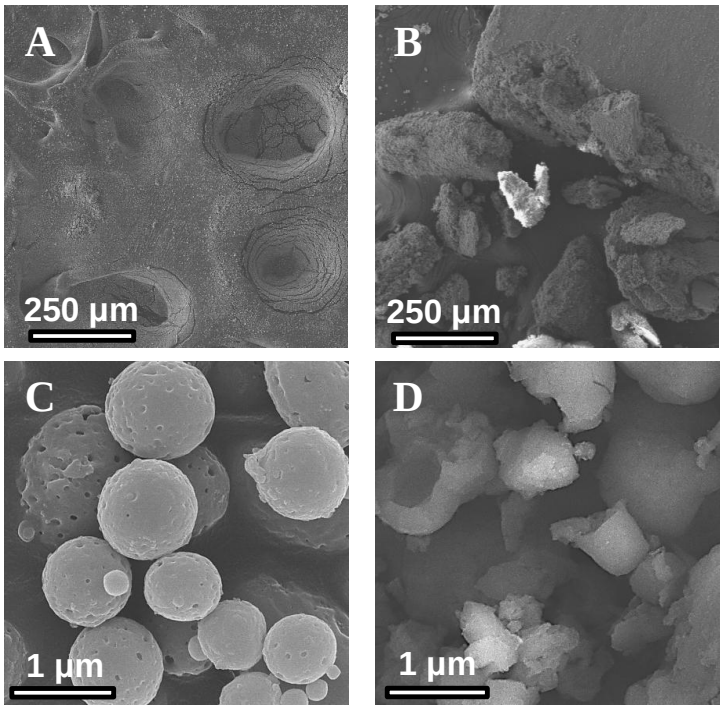

Figure 3.11 SEM images of the USP $CaCO_3$ sorbent. **(A)** Low magnification before cycling. **(B)** Low magnification after 15 cycles. **(C)** High magnification before cycling. **(D)** High magnification after 15 cycles.

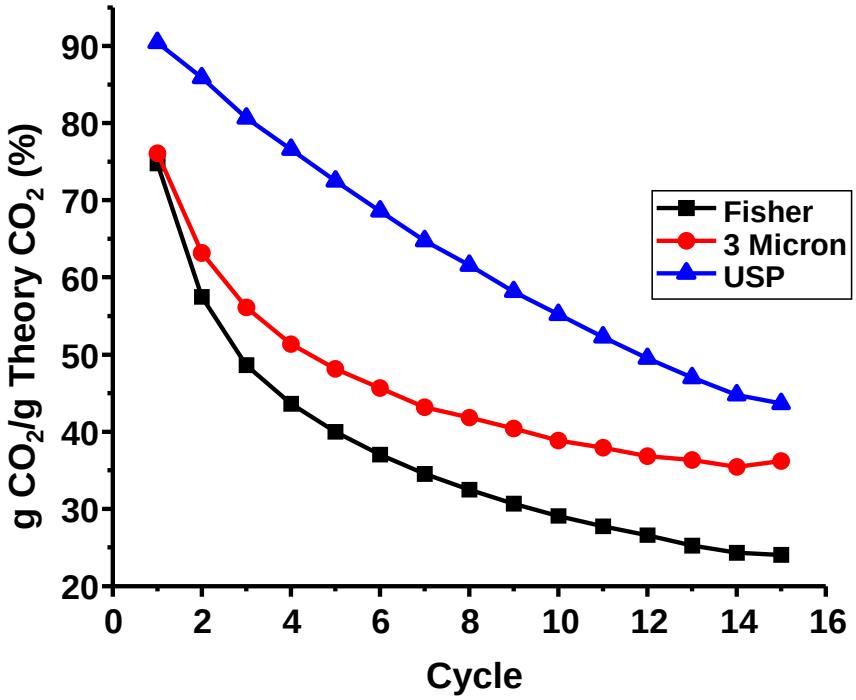

Figure 3.12 Sorbent stability of USP $CaCO_3$ compared to two commercial $CaCO_3$ samples.

3.3.3 CaO Sorbents Synthesized with Binders

3.3.3.1 Mayenite Binder

Mayenite ($Ca_{12}Al_{14}O_{33}$) was added as a binder to the sorbent o overcome the loss of capacity due to sintering and pore-filling of USP CaO. Each sorbent in this section will be described according to the weight ratios of CaO to $Ca_{12}Al_{14}O_{33}$, e.g., the 75:25 Al-sorbent contains a 75:25 w/w ratio of CaO:$Ca_{12}Al_{14}O_{33}$.

XRD of the product isolated from the USP bubblers of the 75:25 Al-sorbent shows only calcite peaks, which is the stable form of $CaCO_3$ at room temperature (Figure 3.13 A). However, XRD taken after the 75:25 Al-sorbent was calcined at 900 °C for 1.5 hours under air shows CaO peaks as well as mayenite peaks (Figure 3.13 B). These results suggest that the aluminum oxide in the Al-containing sorbents exists as an amorphous phase when the product is collected from the bubblers. Under calcining conditions (900 °C), the aluminum forms an inert, stable, and crystalline mayenite phase. The presence of the aluminum phase reduced the $CaCO_3$ crystallite size from 1332 Å to 445 Å. Smaller crystallites are beneficial for carbonation because CO_2 diffuses along grain boundaries to react with the interior of the particle. For cycling tests, the powder is isolated from the USP bubblers and placed in the TGA with no additional pretreatments; calcination of the sorbent prior to XRD was purely for characterization purposes.

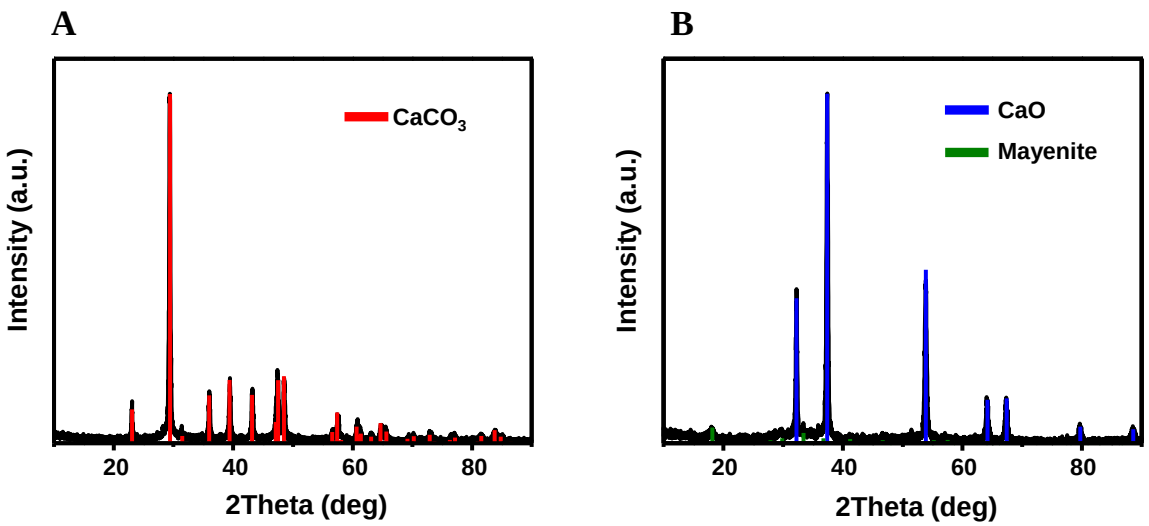

Figure 3.13 XRD patterns of 75:25 Al-sorbent **(A)** before and **(B)** after calcination.

Elemental analysis showed that the amounts of Al, Ca, and C matched the expected theoretical values in all samples except the 0:100 Al-sorbent (Table 3.3). The XRD revealed that there were actually three components present (Figure 3.14). The XRD peak intensities indicate that the majority of the material is mayenite, but there was also a metastable calcium aluminate ($CaAl_2O_4$) and CaO present.

Sorbent	Aluminum (%)	Calcium (%)	Carbon (%)
100:0	N/A	40.84	12.14
95:5	0.8	40.26	11.53
85:15	2.46	37.72	10.4
75:25	4.06	39.01	9.84
65:35	5.71	37.76	9.56
50:50	8.74	35.8	8.37
35:65	11.79	33.2	7.67
0:100	18.73	24.04	6.18

Table 3.3 Elemental analysis results for the Al-containing sorbent series.

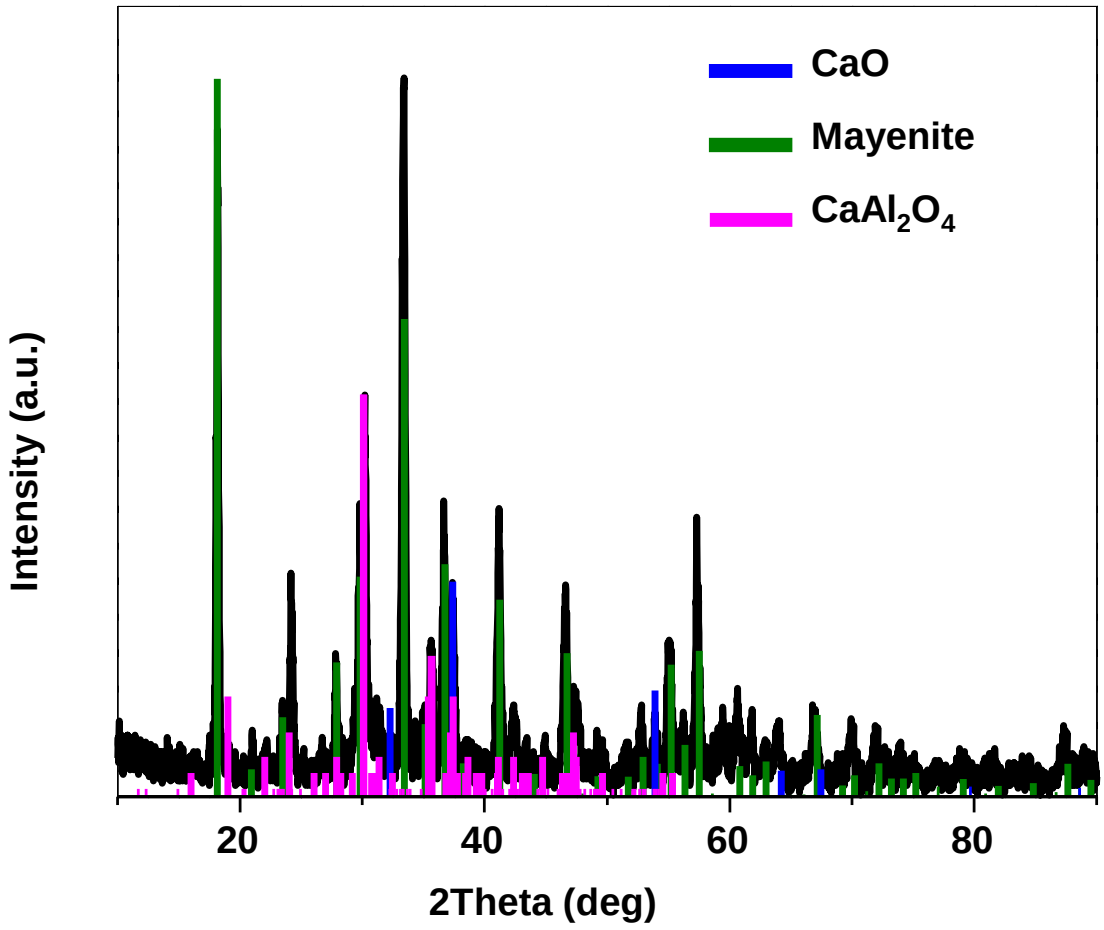

Figure 3.14 XRD of the 0:100 Al-sorbent.

TEM images reveal that there is little correlation between the CaO:$Ca_{12}Al_{14}O_{33}$ ratio and the particle structure (Figure 3.15). The addition of just 5 wt% $Ca_{12}Al_{14}O_{33}$ makes the particles denser and all of the Al-containing sorbents appear denser than pure $CaCO_3$. Each sorbent, however, is still visibly composed of macroporous particles.

The BET surface area of the 35:65 Al-sorbent was 46 m^2/g, and the surface areas of the other sorbents were ~20 m^2/g (Table 3.4). The high surface area of the 35:65 Al-sorbent was likely a result of the high aluminum nitrate concentration in the precursor solution ($Al(NO_3)_3$ has one more mole of nitrate than $Ca(NO_3)_2$ per mole); the extra nitrate likely creates more pores because more gas is evolved during decomposition. The

surface areas of all sorbents except the 35:65 Al-sorbent increased after calcination at 900 °C for 30 min. in air because the volume of $CaCO_3$ is 2.2 times that of CaO, and the removal of CO_2 opens more pores. The high surface area of the 35:65 Al-sorbent decreased after calcination likely due to the collapse of the pore structure induced by the elevated temperature.

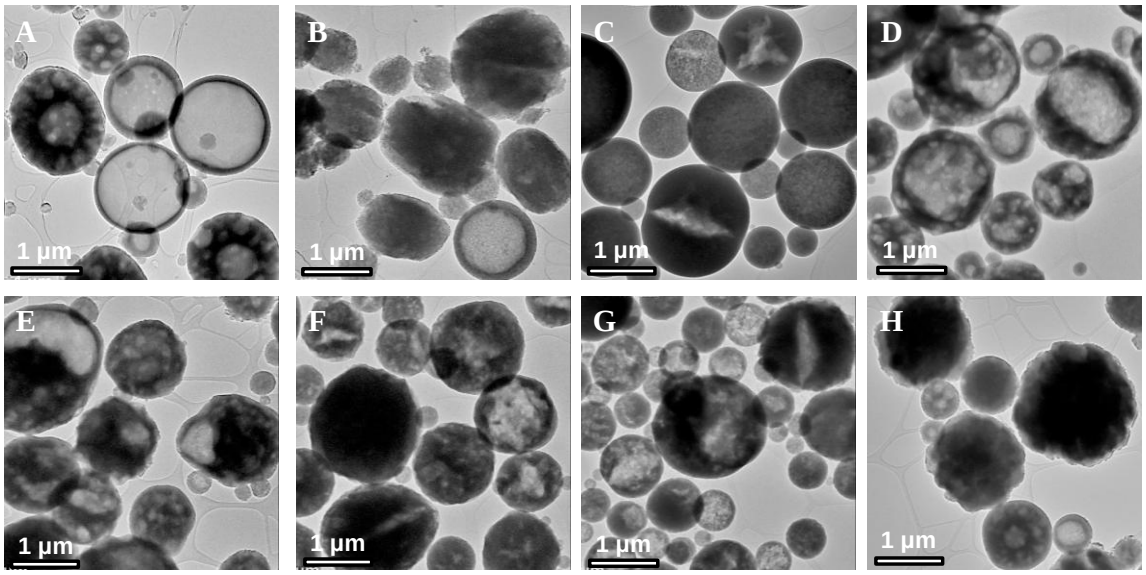

Figure 3.15 TEM images of Al-containing sorbents with various CaO:$Ca_{12}Al_{14}O_{33}$ wt% ratios. **(A)** 100:0. **(B)** 95:5. **(C)** 85:15. **(D)** 75:25. **(E)** 65:35. **(F)** 50:50. **(G)** 35:65. **(H)** 0:100.

Sorbent	**Pre-calcine SA m^2/g**	**Post-calcine SA m^2/g**
95:5	19.583	27.159
85:15	20.387	29.120
75:25	19.847	22.708
65:35	23.684	26.161
50:50	15.861	19.034
35:65	46.411	33.903

Table 3.4 BET surface area analysis of the Al-containing sorbents before and after calcination.

Each of the Al-containing sorbents was cycled using Method 4 (Section 3.3.1.4). As expected, there was a correlation between the initial capacity of each sorbent and the CaO content in the sorbent: sorbents with higher CaO contents initially had higher capacities. Each sorbent demonstrated a loss of capacity over the 15 cycles (Figure 3.16 A), which can be attributed to sintering of the particles. SEM images of the 75:25 Al-sorbent (representative of all Al-sorbents) before cycling, after 2 cycles, and after 15 cycles clearly show progressive agglomeration of the particles (Figure 3.17 A, B, and C). Higher magnification images of the surface of the sintered particle reveal that the original spherical structure is still intact after 2 cycles and spheres are still visible after 15 cycles (Figure 3.17 D, E, and F), which suggests that the mayenite binder offers structural support to the sorbent. The pure USP $CaCO_3$ sorbent lost nearly all of the original spherical shape (Figure 3.11).

There is a very obvious initial increase in sorbent stability for the 50:50 Al-sorbent and the 35:65 Al-sorbent (Figure 3.16 B). The mayenite phase forms slowly during the first few calcinations and, as it does, makes more CaO available for CO_2 capture. The cycling data showed that the 75:25 Al-sorbent is the most stable and retains the highest capacity after 15 cycles.

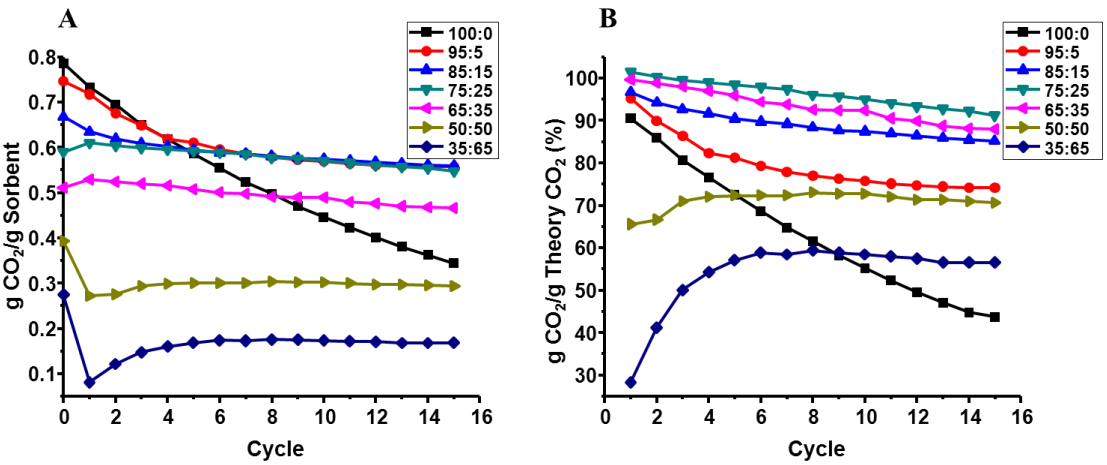

Figure 3.16 Graphs of the Al-containing sorbents showing **(A)** sorbent capacity and **(B)** sorbent stability over 15 cycles. Cycle zero represents the theoretical capacity.

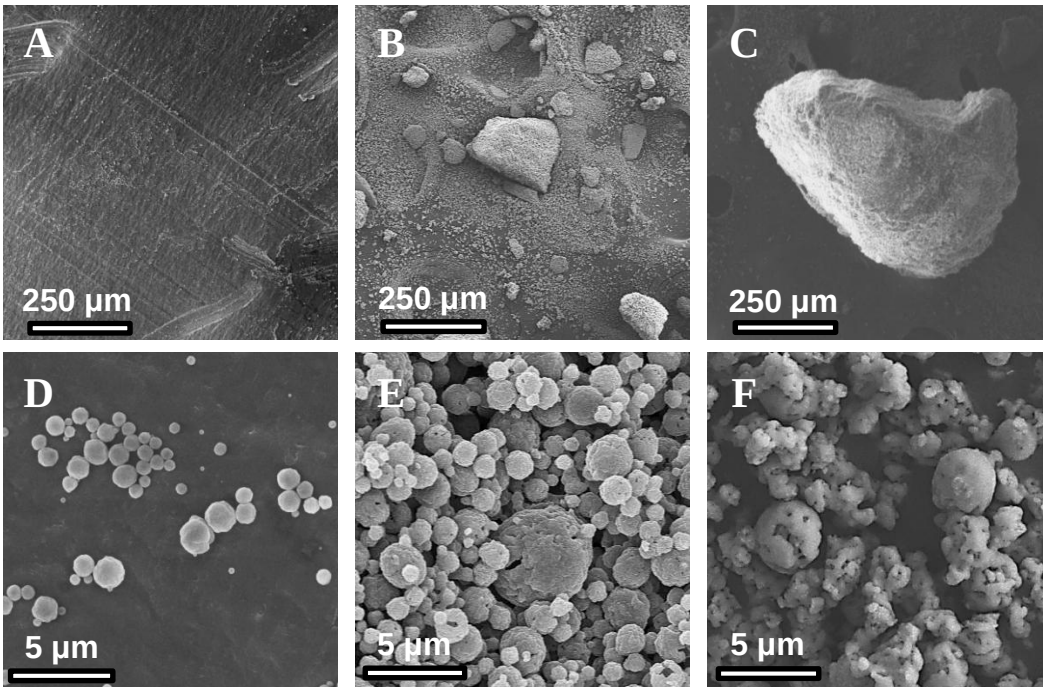

Figure 3.17 SEM images of the 75:25 Al-sorbent. **(A)** Low magnification before cycling. **(B)** Low magnification after 15 cycles. **(C)** High magnification before cycling. **(D)** High magnification after 15 cycles.

Both capacity and stability are necessary metrics for complete analysis of the sorbents. For example, the 65:35 Al-sorbent shows a moderate capacity of about 0.5 g CO_2/g sorbent but excellent stability over the course of 15 cycles, which indicates that the

65:35 Al-sorbent could be a potential sorbent for cycle numbers significantly larger than 15 (i.e. hundreds of cycles). The 95:5, 85:15, and 75:25 Al-sorbents captured the most CO_2 per gram of sorbent after 15 cycles (Figure 3.18). The 75:25 Al-sorbent was the most stable over 15 cycles, however all three sorbents have the same capacity after 15 cycles, which makes it difficult to predict which sorbent will perform the best over long cycles. In general, the literature reports that the higher binder content sorbents tend to be the most stable over long cycles.[28, 29]

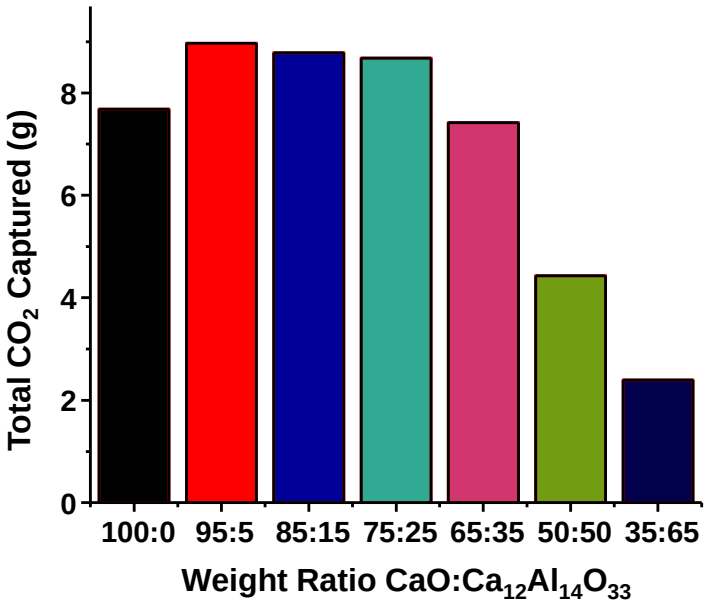

Figure 3.18 Total CO_2 captured per gram of each Al-containing sorbent.

3.3.3.2 Magnesium Oxide Binder

Magnesium oxide was also used as a binder to improve sorbent stability. TEM images of the 75:25 w/w CaO:MgO product show that the particles are ruffled, porous spheres. These pores alleviate strain from particle expansion during carbonation. XRD showed the MgO was amorphous after USP at 600 °C (Figure 3.19), but elemental analysis for Ca, Mg, and C matched the theoretical values, which confirmed the presence

of the MgO. The presence of the MgO binder caused the $CaCO_3$ crystallite size to decrease from 1332 Å to 750 Å, which produces more grain boundaries through which CO_2 can diffuse and improves sorbent stability.

Cycling the 75:25 Mg-sorbent on the TGA 15 times demonstrated that this sorbent is has higher stability and capacity compared to pure USP $CaCO_3$ (Figure 3.20). However, the 75:25 Al-sorbent discussed in section 3.3.3.1 showed better performance than the 75:25 Mg-sorbent.

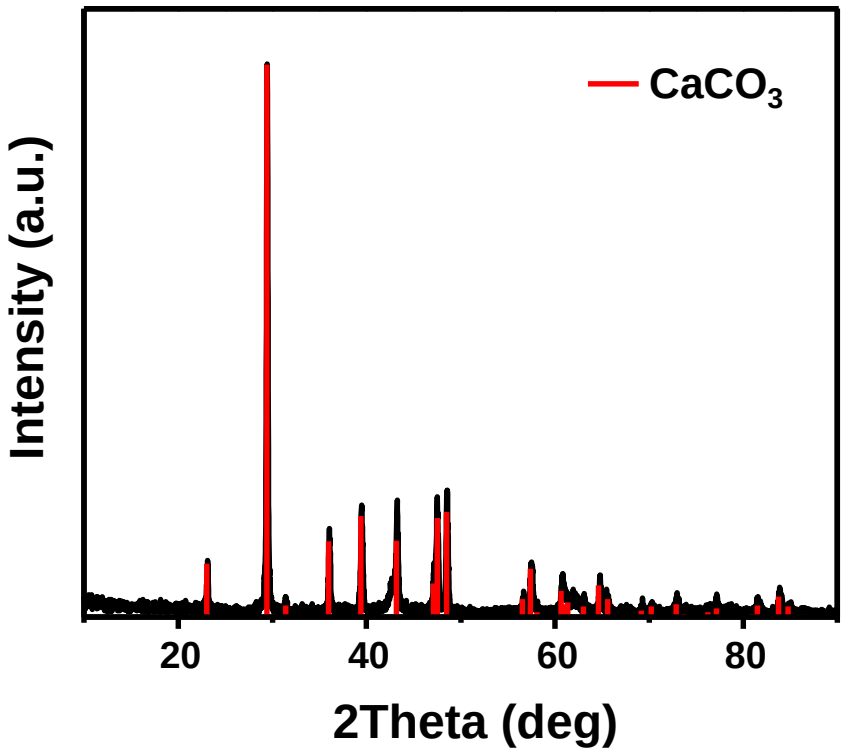

Figure 3.19 XRD of the 75:25 Mg-sorbent.

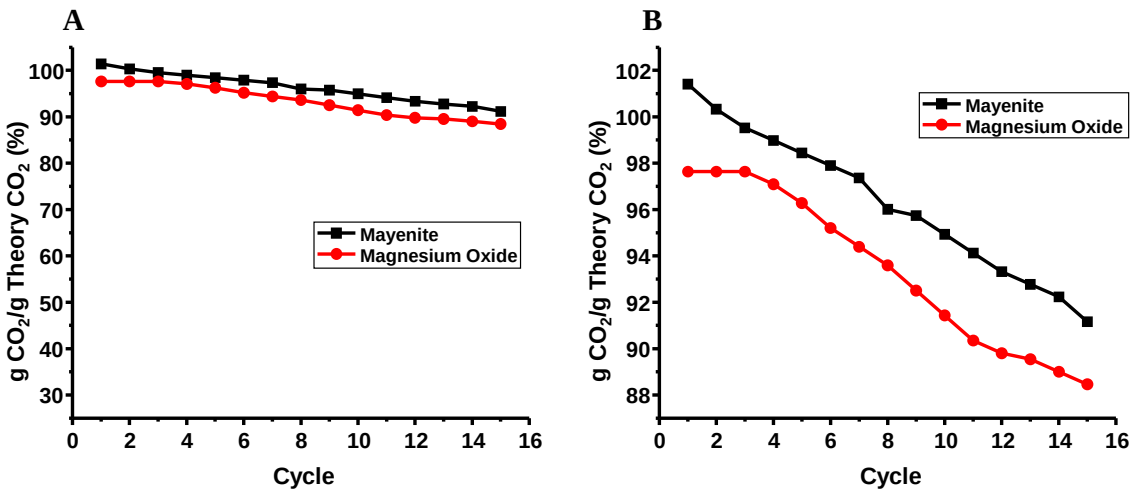

Figure 3.20 (A) Comparison of the 75:25 Al-sorbent and the 75:25 Mg-sorbent. **(B)** Enlarged for clear distinction.

3.4 Summary

USP offers control over the structure of $CaCO_3$ particles. While USP synthesis improves the stability of CaO sorbents over 15 cycles compared to commercially available calcium carbonate, the hollow structure is still unable to fully accommodate the volume change and sintering effects that occur over multiple calcination/carbonation cycles to make pure $CaCO_3$ an industrially viable sorbent. Consequently, inert binders must be added to improve sorbent stability over multiple cycles. Al- and Mg-containing binders were investigated and found to greatly enhance the sorbent stability and reduce the sintering effects. The 75:25 Al-containing sorbent was shown to be the most stable sorbent however it is difficult to predict whether the 75:25, 85:15, or 95:5 Al-containing sorbent will perform best when the number of cycles is significantly increased beyond 15.

3.5 References

1. Choi, S.; Drese, J. H.; Jones, C. W. Adsorbent Materials for Carbon Dioxide Capture from Large Anthropogenic Point Sources. *ChemSusChem* **2009,** *2,* 796-854.

2. Blamey, J.; Paterson, N. P. M.; Dugwell, D. R.; Fennell, P. S. Mechanism of Particle Breakage during Reactivation of CaO-Based Sorbents for CO2 Capture. *Energ. Fuel.* **2010,** *24*, 4605-4616.

3. Barker, R. The reversibility of the reaction CaCO3 ⇄ CaO+CO2. *J. Appl Chem Biotechn.* **1973,** *23*, 733-742.

4. Barker, R. The reactivity of calcium oxide towards carbon dioxide and its use for energy storage. *J. Appl Chem Biotechn.* **1974,** *24*, 221-227.

5. Mess, D.; Sarofim, A. F.; Longwell, J. P. Product layer diffusion during the reaction of calcium oxide with carbon dioxide. *Energ. Fuel.* **1999,** *13*, 999-1005.

6. Gupta, H.; Fan, L. S. Carbonation-calcination cycle using high reactivity calcium oxide for carbon dioxide separation from flue gas. *Ind. Eng. Chem. Res.* **2002,** *41*, 4035-4042.

7. Lu, H.; Reddy, E. P.; Smirniotis, P. G. Calcium oxide based sorbents for capture of carbon dioxide at high temperatures. *Ind. Eng. Chem. Res.* **2006,** *45*, 3944-3949.

8. Yang, Z.; Zhao, M.; Florin, N. H.; Harris, A. T. Synthesis and Characterization of CaO Nanopods for High Temperature CO2 Capture. *Ind. Eng. Chem. Res.* **2009,** *48*, 10765-10770.

9. Grasa, G. S.; Abanades, J. C. CO2 capture capacity of CaO in long series of carbonation/calcination cycles. *Ind. Eng. Chem. Res.* **2006,** *45*, 8846-8851.

10. Lysikov, A. I.; Salanov, A. N.; Okunev, A. G. Change of CO2 carrying capacity of CaO in isothermal recarbonation-decomposition cycles. *Ind. Eng. Chem. Res.* **2007,** *46*, 4633-4638.

11. Grasa, G.; Gonzlaez, B.; Alonso, M.; Abanades, J. C. Comparison of CaO-Based Synthetic CO2 Sorbents under Realistic Calcination Conditions. *Energ. Fuel.* **2007,** *21*, 3560-3562.

12. Abanades, J. C. The maximum capture efficiency of CO2 using a carbonation/calcination cycle of CaO/CaCO3. *Chem. Eng. J.* **2002,** *90*, 303-306.

13. Abanades, J. C.; Alvarez, D. Conversion limits in the reaction of CO2 with lime. *Energ. Fuel.* **2003,** *17*, 308-315.

14. Manovic, V.; Anthony, E. J. Sintering and Formation of a Nonporous Carbonate Shell at the Surface of CaO-Based Sorbent Particles during CO2-Capture Cycles. *Energ. Fuel.* **2010,** *24*, 5790-5796.

15. Sun, P.; Grace, J. R.; Lim, C. J.; Anthony, E. J. The effect of CaO sintering on cyclic CO2 capture in energy systems. *Aiche J.* **2007,** *53*, 2432-2442.

16. Wang, J. S.; Anthony, E. J. On the decay behavior of the CO2 absorption capacity of CaO-based sorbents. *Ind. Eng. Chem. Res.* **2005,** *44*, 627-629.

17. Li, L.; King, D. L.; Nie, Z.; Li, X. S.; Howard, C. MgAl2O4 Spinel-Stabilized Calcium Oxide Absorbents with Improved Durability for High-Temperature CO2 Capture. *Energ. Fuel.* **2010,** *24*, 3698-3703.

18. Curran, G. P.; Fink, C. E.; Gorin, E. CO_2 Acceptor Gasification Process: Studies of Acceptor Properties. *Adv. Chem. Ser.* **1967,** *69*, 141-165.

19. Silaban, A.; Harrison, D. P. High temperature capture of carbon dioxide: Characteristics of the reversible reaction between CaO(s) and CO2(g). *Chem. Eng. Commun.* **1995,** *137*, 177-190.

20. Aihara, M.; Nagai, T.; Matsushita, J.; Negishi, Y.; Ohya, H. Development of porous solid reactant for thermal-energy storage and temperature upgrade using carbonation/decarbonation reaction. *Appl. Energ.* **2001,** *69*, 225-238.

21. Shimizu, T.; Hirama, T.; Hosoda, H.; Kitano, K.; Inagaki, M.; Tejima, K. A twin fluid-bed reactor for removal of CO2 from combustion processes. *Chem. Eng. Res. Des.* **1999,** *77*, 62-68.

22. Deutsch, Y.; Hellerkallai, L. Decarbonation and recarbonation of calcites heated in CO2 .1. Effect of the Thermal Regime. *Thermochim. Acta.* **1991,** *182*, 77-89.

23. Bhatia, S. K.; Perlmutter, D. D. Effect of the product layer on the kinetics of the CO2-lime reaction. *Aiche J.* **1983,** *29*, 79-86.

24. Feng, B.; Liu, W.; Li, X.; An, H. Overcoming the Problem of Loss-in-Capacity of Calcium Oxide in CO2 Capture. *Energ. Fuel.* **2006,** *20*, 2417-2420.

25. Huang, C. H.; Chang, K. P.; Yu, C. T.; Chiang, P. C.; Wang, C. F. Development of high-temperature CO2 sorbents made of CaO-based mesoporous silica. *Chem. Eng. J.* **2010,** *161*, 129-135.

26. Wu, Z. X.; Hao, N.; Xiao, G. K.; Liu, L. Y.; Webley, P.; Zhao, D. Y. One-pot generation of mesoporous carbon supported nanocrystalline calcium oxides capable of efficient CO2 capture over a wide range of temperatures. *Phys. Chem. Chem. Phys. 13*, 2495-2503.

27. Florin, N. H.; Blamey, J.; Fennell, P. S. Synthetic CaO-Based Sorbent for CO2 Capture from Large-Point Sources. *Energ. Fuel.* **2010,** *24*, 4598-4604.

28. Li, Z. S.; Cai, N. S.; Huang, Y. Y. Effect of preparation temperature on cyclic CO2 capture and multiple carbonation-calcination cycles for a new Ca-based CO2 sorbent. *Ind. Eng. Chem. Res.* **2006,** *45*, 1911-1917.

29. Li, Z. S.; Cai, N. S.; Huang, Y. Y.; Han, H. J. Synthesis, experimental studies, and analysis of a new calcium-based carbon dioxide absorbent. *Energ. Fuel.* **2005,** *19*, 1447-1452.

30. Liu, W.; Feng, B.; Wu, Y.; Wang, G.; Barry, J.; Diniz da Costa, J. C. Synthesis of Sintering-Resistant Sorbents for CO2 Capture. *Environ. Sci. Technol.* **2010,** *44*, 3093-3097.

31. Lu, H.; Khan, A.; Pratsinis, S. E.; Smirniotis, P. G. Flame-Made Durable Doped-CaO Nanosorbents for CO2 Capture. *Energ. Fuel.* **2008,** *23*, 1093-1100.

32. Luo, C.; Zheng, Y.; Ding, N.; Wu, Q. L.; Bian, G. A.; Zheng, C. G. Development and Performance of CaO/La2O3 Sorbents during Calcium Looping Cycles for CO2 Capture. *Ind. Eng. Chem. Res.* **2010,** *49*, 11778-11784.

33. Manovic, V.; Anthony, E. J. CaO-Based Pellets Supported by Calcium Aluminate Cements for High-Temperature CO2 Capture. *Environ. Sci. Technol.* **2009,** *43*, 7117-7122.

34. Martavaltzi, C. S.; Lemionidou, A. A. Parametric Study of the CaO-Ca12Al14O33 Synthesis with Respect to High CO2 Sorption Capacity and Stability on Multicycle Operation. *Ind. Eng. Chem. Res.* **2008,** *47*, 9537-9543.

35. Martavaltzi, C. S.; Pampaka, E. P.; Korkakaki, E. S.; Lemonidou, A. A. Hydrogen Production via Steam Reforming of Methane with Simultaneous CO2 Capture over CaO-Ca12Al14O33. *Energ. Fuel.* **2010,** *24*, 2589-2595.

36. Reddy, E. P.; Smirniotis, P. G. High-temperature sorbents for CO2 made of alkali metals doped on CaO supports. *J. Phys. Chem. B* **2004,** *108*, 7794-7800.

37. Wu, S. F.; Li, Q. H.; Kim, J. N.; Yi, K. B. Properties of a nano CaO/Al2O3 CO2 sorbent. *Ind. Eng. Chem. Res.* **2008,** *47*, 180-184.

38. Martavaltzi, C. S.; Pefkos, T. D.; Lemonidou, A. A. Operational Window of Sorption Enhanced Steam Reforming of Methane over CaO-Ca12Al14O33. *Ind. Eng. Chem. Res.* **2011,** *50*, 539-545.

39. Wu, S. F.; Jiang, M. Z. Formation of a Ca12Al14O33 Nanolayer and Its Effect on the Attrition Behavior of CO2-Adsorbent Microspheres Composed of CaO Nanoparticles. *Ind. Eng. Chem. Res.* **2010,** *49*, 12269-12275.

40. Kuramoto, K.; Fujimoto, S.; Morita, A.; Shibano, S.; Suzuki, Y.; Hatano, H.; Lin, S. Y.; Harada, M.; Takarada, T. Repetitive carbonation-calcination reactions of Ca-based sorbents for efficient CO2 sorption at elevated temperatures and pressures. *Ind. Eng. Chem. Res.* **2003,** *42*, 975-981.

41. Manovic, V.; Anthony, E. J. Reactivation and remaking of calcium aluminate pellets for CO2 capture. *Fuel* **2011,** *90*, 233-239.

42. Materic, V.; Sheppard, C.; Smedley, S. I. Effect of Repeated Steam Hydration Reactivation on CaO-Based Sorbents for CO2 Capture. *Environ. Sci. Technol.* **2010,** *44*, 9496-9501.

43. Wang, Y.; Lin, S. Y.; Suzuki, Y. Experimental study on CO2 capture conditions of a fluidized bed limestone decomposition reactor. *Fuel Process. Technol.* **2010,** *91*, 958-963.

44. Brockner, W.; Ehrhardt, C.; Gjikaj, M. Thermal decomposition of nickel nitrate hexahydrate, Ni(NO3)2·6H2O, in comparison to Co(NO3)2·6H2O and Ca(NO3)2·4H2O. *Thermochim. Acta.* **2007,** *456*, 64-68.

45. Qi, L. M.; Li, J.; Ma, J. M. Biomimetic morphogenesis of calcium carbonate in mixed solutions of surfactants and double-hydrophilic block copolymers. *Adv. Mater.* **2002,** *14*, 300-303.

46. Dong, W.; Cheng, H.; Yao, Y.; Zhou, Y.; Tong, G.; Yan, D.; Lai, Y.; Li, W. Bioinspired Synthesis of Calcium Carbonate Hollow Spheres with a Nacre-Type Laminated Microstructure. *Langmuir* **2011,** *27*, 366-370.

47. Bastakoti, B. P.; Guragain, S.; Yokoyama, Y.; Yusa, S.-i.; Nakashima, K. Synthesis of Hollow CaCO3 Nanospheres Templated by Micelles of Poly(styrene-b-acrylic acid-b-ethylene glycol) in Aqueous Solutions. *Langmuir* **2011,** *27*, 379-384.